Solid Earth

Open Access

EGU

The link between Somalian Plate rotation and the East African Rift System: an analogue modelling study

Frank Zwaan[1,2,3] **and Guido Schreurs**[1]

[1]Institute of Geological Sciences, University of Bern, Baltzerstrasse 1+3, 3012 Bern, Switzerland
[2]Helmholtz Centre Potsdam – GFZ German Research Centre for Geosciences, Telegrafenberg, 14473 Potsdam, Germany
[3]Department of Geosciences, University of Fribourg, Chemin du Musée 6, 1700 Fribourg, Switzerland

Correspondence: Frank Zwaan (frank.zwaan@gfz-potsdam.de)

Abstract. The East African Rift System (EARS) represents a major tectonic feature that splits the African continent between the Nubian Plate situated to the west and the Somalian Plate to the east. The EARS comprises various rift segments and microplates and represents a key location for studying rift evolution. Researchers have proposed various scenarios for the evolution of the EARS, but the impact of continent-scale rotational rifting, linked to the rotation of the Somalian Plate, has received only limited attention. In this study we apply analogue models to explore the dynamic evolution of the EARS within its broader rotational-rifting framework. Our models show that rotational rifting leads to the lateral propagation of deformation towards the rotation axis, which reflects the general southward propagation of the EARS. However, we must distinguish between the propagation of distributed deformation, which can move very rapidly, and localized deformation, which can significantly lag behind the former. The various structural-weakness arrangements in our models (simulating the pre-existing lithospheric heterogeneities that localize rifting along the EARS) lead to a variety of structures. Laterally overlapping weaknesses are required for localizing parallel rift basins to create rift pass structures, leading to the rotation and segregation of microplates such as the Victoria Plate in the EARS, as well as to the simultaneous north- and southward propagation of the adjacent Western Rift. Additional model observations concern the development of early pairs of rift-bounding faults flanking the rift basins, followed by the localization of deformation along the axes of the most developed rift basins. Furthermore, the orientation of rift segments with respect to the regional (rotational) plate divergence affects deformation along these segments: oblique rift segments are less wide due to a strike-slip deformation component. Overall, our model results generally fit the large-scale present-day features of the EARS, with implications for general rift development and for the segregation and rotation of the Victoria Plate.

1 Introduction

The East African Rift System (EARS) forms a major plate tectonic feature that splits the African continent into two main domains, with the western domain belonging to the Nubian Plate and the eastern domain belonging to the Somalian Plate (e.g. Morley et al., 1999; Chorowicz, 2005; Ring, 2014; Saria et al., 2014; Macgregor, 2015; Fig. 1a and b). From its northern end in the Afar Triangle, where the rift merges with the Red Sea and Gulf of Aden basins, the EARS stretches some 5000 km southward and comprises various active rift segments that are arranged in two main branches in the (north-)east and (south-)west (e.g. Ebinger, 1989; Chorowicz, 2005; Corti, 2012; Stamps et al., 2008, 2014, 2021; Saria et al., 2013, 2014; Daly et al., 2020; Michon et al., 2022; Martin, 2023; Fig. 1a and b). The eastern branch contains the Main Ethiopian Rift and the Kenya Rift, whereas the western branch consists of the Western Rift with its various sub-basins and the Malawi Rift to the south. These two main branches encompass the Victoria microplate, whereas another less active rift zone following part of the offshore Davie Fracture Zone defines the eastern limit of the Rovuma microplate, which is bounded by the Malawi Rift to its west. A third microplate, the Lwandle Plate, is situated
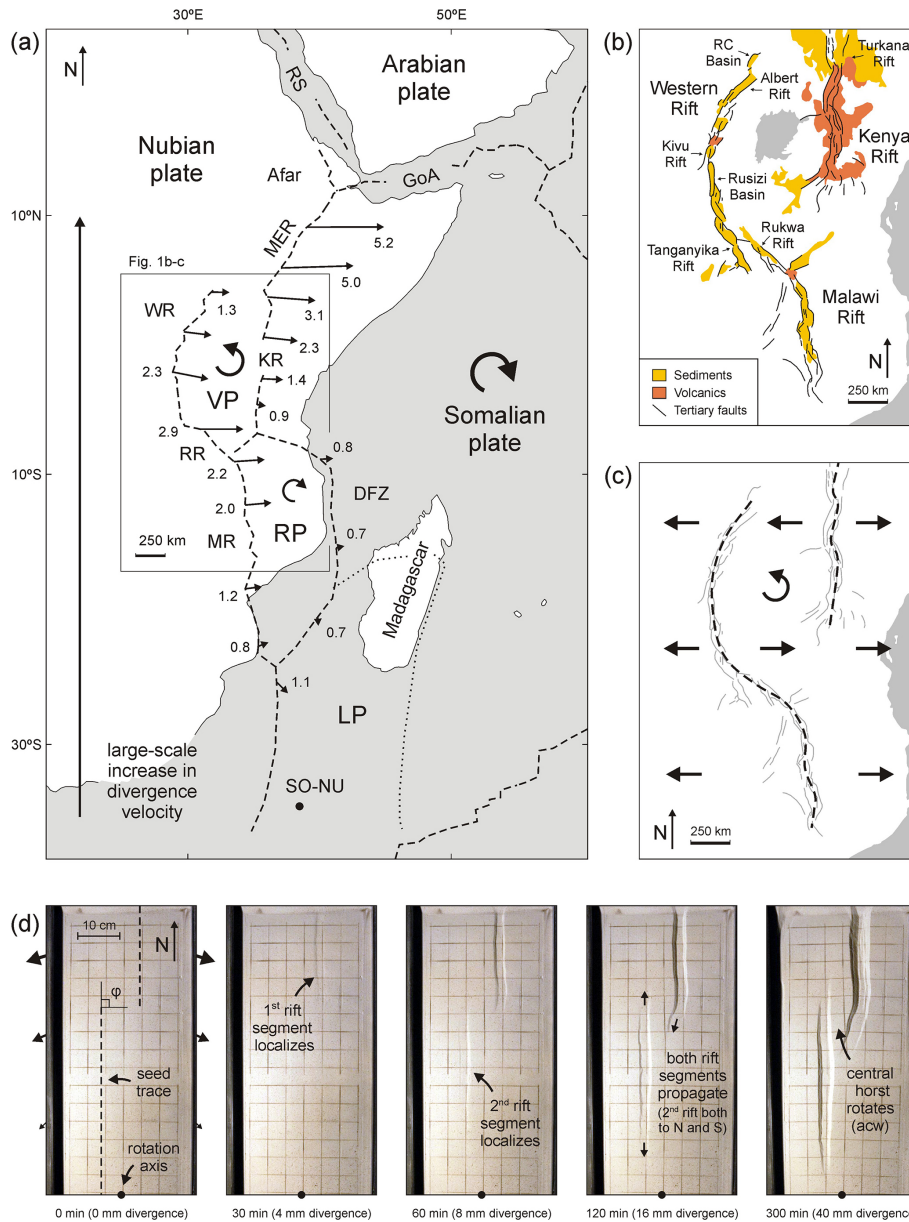
Figure 1. (a) Tectonic outline of the East African Rift System (EARS) showing the rotation of the Somalian Plate, the Victoria Plate (VP), and the Rovuma Plate (RP). Plate motions (mm yr^{-1}); dotted lines indicate plate boundaries. Modified after Saria et al. (2013, 2014) and Stamps et al. (2021). DFZ: Davie Fracture Zone; GoA: Gulf of Aden; KR: Kenya Rift; LP: Lwandle Plate; MER: Main Ethiopian Rift; MR: Malawi Rift; RC: Rhino Camp Basin; RP: Rovuma Plate; RR: Rukwa Rift; RS: Red Sea; SO–NU: Somalia–Nubia rotation pole; WR: Western Rift. **(b)** Detailed structural map of the EARS. Modified after Ebinger (1989). **(c)** Tectonic model proposed for the EARS; after Glerum et al. (2020). **(d)** Analogue models of rift interaction in a rotational-rifting setting by Zwaan and Schreurs (2020). Acw: anticlockwise; φ: angle between the seed (i.e. inherited weakness) orientation and the line between both seed tips (90° in this case, i.e. no lateral seed overlap).

farther south. The EARS is a key location for the study of rift evolution as it contains rift basins in different stages of development, from young continental rift basins in the south to (incipient) continental break-up in the northernmost Ethiopian Rift and the Afar Triangle (e.g. Chorowicz, 2005; Ebinger, 2005; Corti, 2012; Macgregor; 2015; Fig. 1a and b).

The development of the present-day EARS is thought to have started some 28 Myr ago in the Turkana part of the Kenya Rift (Fig. 1b), following earlier phases of mantle-induced volcanism, and researchers have proposed different scenarios for the subsequent evolution of the rift system (e.g. Chorowicz, 2005; Morley, 2010; Macgregor, 2015; Purcell, 2018; Glerum et al., 2020; Martin, 2023). According to some

authors, large-scale NW–SE plate divergence caused rifting along the various rift segments, with large offsets between the Western Rift and Kenya Rift, as well as between the Western Rift and Malawi Rift (i.e. along the Rukwa Rift), being accommodated by large-scale NW–SE-oriented strike-slip zones (e.g. Wheeler and Karson, 1994; Scott et al., 1989; Chorowicz, 2005). Other authors have favoured general E–W plate divergence along the EARS (e.g. Lezzar et al., 2002; Morley, 2010; Delvaux et al., 2012), which is more in line with present-day GPS observations (e.g. Calais et al., 2006; Saria et al., 2013, 2014; Stamps et al., 2021). In general, the localization of the rift basins is thought to be controlled by the arrangement of inherited lithospheric weaknesses such as the Proterozoic Pan-African structural grain or the Mesozoic Davie Fracture Zone, which are more readily reactivated during tectonic deformation than undisturbed or cratonic lithosphere (e.g. Ring, 2014; Kendall and Lithgow-Bertelloni, 2016; Phethean et al., 2016; Michon et al., 2022; Kolawole et al., 2021a, b; and references therein). The exact timing of rift initiation in the different parts of the EARS remains debated, although the general trend is reported to be one of southward younging over the past ca. 30 Myr (e.g. Chorowicz, 2005; Macgregor, 2015; Michon et al., 2022; Martin, 2023; and references therein).

An important aspect of the present-day EARS is rotational plate motion, with Martin (2023) highlighting the opposite rotations of the Victoria and Rovuma plates (Fig. 1a). Numerical modelling efforts by Glerum et al. (2020) suggest that the anticlockwise rotation of the Victoria Plate occurs due to general E–W extension acting on the overlapping branches of the EARS (i.e. the western and eastern branches) that cause the Victoria Plate in between them to rotate in an anticlockwise fashion (forming a so-called "rift pass" structure; e.g. Oldenburg and Brune, 1975; Nelson et al., 1992; Hieronymus, 2004; Katz et al., 2005; Tentler and Acocella, 2010; Brune et al., 2017; Zwaan et al., 2018a; Kolawole et al., 2021a; Fig. 1c). Glerum et al. (2020) also demonstrate that mantle flow linked to mantle plume activity below the generally magma-rich EARS (e.g. Macgregor, 2015; Michon et al., 2022; Rajaonarison et al., 2023; and references therein) is not required to drive Victoria Plate rotation, since a far-field mechanism would suffice to explain tectonic deformation along the EARS. Yet, the forces driving rifting along the EARS remain hotly debated (e.g. Kendall and Lithgow-Bertelloni, 2016; Rajaonarison et al., 2021; Martin, 2023; and references therein).

On a larger scale, we observe the present-day clockwise rotation of the Somalian Plate (e.g. Saria et al., 2013, 2014; Stamps et al., 2021), which has been occurring since at least 20 Ma (DeMets and Merkouriev, 2016, 2021), and the associated southward decrease in general E–W plate divergence along the EARS (Fig. 1a). Tectonic modelling studies have shown that such plate divergence gradients have important effects on the evolution and propagation of rift systems (e.g. Souriot and Brun, 1992; Benes and Scott, 1996;

Sun et al., 2009; Molnar et al., 2017, 2018; Mondy et al., 2018; Farangitakis et al., 2019, 2021; Khalil et al., 2020; Zwaan et al., 2020; Schmid et al., 2022a). Although Glerum et al. (2020) did incorporate a gradual southward in-plate divergence velocity decrease into their models, they only focussed on the immediate surroundings of the Victoria Plate (Fig. 1c). Recently, Zwaan and Schreurs (2020) presented a first-order analogue modelling study exploring the rift interaction structures in rotational and orthogonal rifting settings (Fig. 1d). Their model results suggested that large-scale rotational rifting explained the large-scale southward younging trend of the rift system, as reported by, for example, Chorowicz (2005) and Macgregor (2015). However, Zwaan and Schreurs (2020) concentrated on systematically testing generic rift arrangements and presented a qualitative model analysis based on visual inspection of time-lapse imagery so that a comparison of their models to the EARS remains rather coarse (Fig. 1d). To our knowledge, no other large-scale (modelling) studies involving rotational rifting focused on the EARS exist in the scientific literature.

Hence, we present here a new series of analogue tectonic models of rotational rifting that are specifically tailored to the tectonic setting in the EARS, with the aim to explore the dynamic evolution of the rift system in more detail. To this end we adopt the general plate configuration of the EARS and the rotational plate motion pattern of the Somalian Plate provided by GPS studies (e.g. Saria et al., 2013, 2014; Stamps et al., 2021) and plate reconstructions (DeMets and Merkouriev, 2016, 2021). We find that our new models generally fit the large-scale features and present-day deformation of the EARS, with implications for general rift development, rift basin propagation, and segregation and rotation of the Victoria Plate.

2 Methods

2.1 Model set-up

In this study we apply a rotational extension set-up with a brittle–viscous layering, based on previous analogue modelling efforts by Zwaan and Schreurs (2020), Zwaan et al. (2020), and Schmid et al. (2022a, b) (Figs. 1d, 2). Prior to model preparation, an 8 cm thick foam block base (RG 50 polyurethane foam from GOBAG; http://www.gobag.ch, last access: 1 July 2023) is compressed between two longitudinal sidewalls, on which the brittle–viscous model materials (1.5 cm quartz sand on top of a 3 cm thick viscous mixture representing a 150 km thick lithosphere and the upper 300 km of the sub-lithospheric mantle, respectively) are applied. One of the sidewalls is mobile and connected to a rotation axis, allowing it to rotate in a clockwise fashion, thus simulating the rotation of the Somalian Plate with respect to the Nubian Plate, in a far-field tectonic setting (Fig. 1). Note that we do not distinguish between continental and oceanic litho-
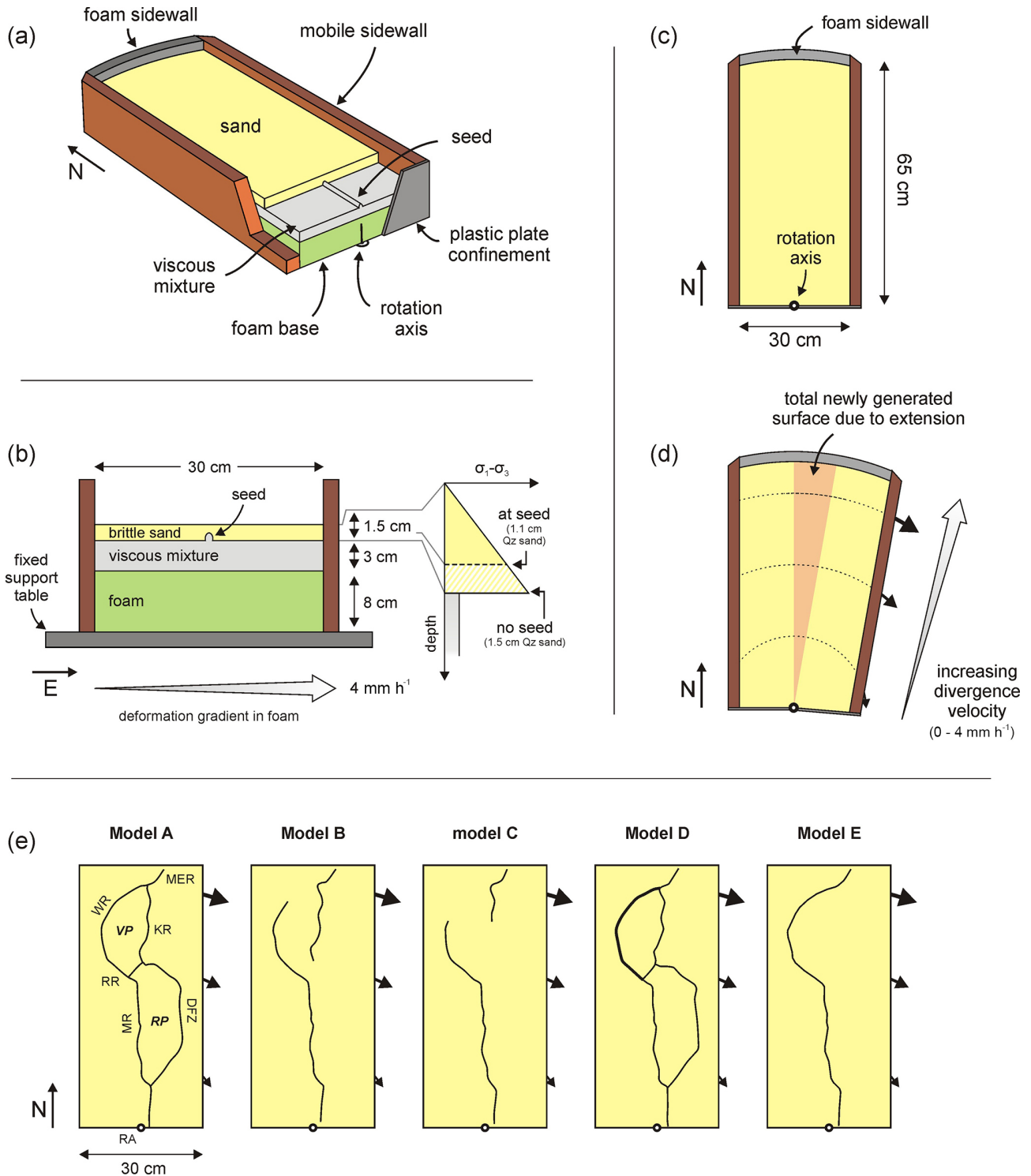
Figure 2. Model set-up. **(a)** Three-dimensional sketch of model set-up. **(b)** Cross-section of model set-up. **(c)** Top view of model set-up prior to deformation and **(d)** after rotational deformation. **(e)** Seed geometries applied for Models A–E, where Model D contains a double-diameter seed along the simulated Western Rift (WR). The seed geometries are based on the rift arrangement in the East African Rift System (EARS), as presented in Fig. 1a and indicated in the panel of Model A. DFZ: Davie Fracture Zone; KR: Kenya Rift; MER: Main Ethiopian Rift; MR: Malawi Rift; RP: Rovuma Plate; RR: Rukwa Rift; VP: Victoria Plate; WR: Western Rift. Note that the rotation axis (RA) is situated somewhat too much to the west when compared to the natural case (Fig. 1a), but this does not affect the model results in any significant fashion (see description of Model F in the Appendix).

Table 1. Model materials.

Granular materials	Quartz sand[a]	Corundum sand[b]
Grain size range	60–250 µm	88–125 µm
Density (bulk material)[c]	2650 kg m^{-3}	3950 kg m^{-3}
Density (sieved)	1560 kg m^{-3}	1890 kg m^{-3}
Angle of internal peak friction	36.1°	37°
Angle of dynamic–stable friction	31.4°	32°
Angle of reactivation friction	33.5°	–
Cohesion	9 ± 98 Pa	39 ± 10 Pa
Viscous materials	**Pure PDMS[a, d]**	**PDMS–corundum sand mixture[a]**
Weight ratio PDMS : corundum sand	–	0.965 kg : 1.00 kg
Density	965 kg m^{-3}	1600 kg m^{-3}
Viscosity	ca. 2.8×10^4 Pa s	ca. 1.5×10^5 Pa s[e]
Rheology[f]	Newtonian ($n = 1$)	Near-Newtonian ($n = 1.05$–1.10)

[a] Quartz sand, PDMS (SGM-36 polydimethylsiloxane), and viscous mixture characteristics after Zwaan et al. (2016, 2018b, c; Schmid et al., 2020). [b] Corundum sand characteristics after Panien et al. (2006). [c] Bulk material densities after Carlo AG (2023). [d] Pure-PDMS rheology after Rudolf et al. (2016). [e] Viscosity value holds for model strain rates $< 10^{-4}$ s^{-1}. [f] Power-law exponent n (dimensionless) represents sensitivity to strain rate.

sphere in our models, assuming that the various plates along the EARS act as rigid blocks (Stamps et al., 2021). During this rotational motion of the mobile sidewall the foam base expands, inducing extension in the overlying model materials with a southwardly decreasing gradient (Fig. 2c and d). The rotational motion of the sidewall is set to a constant divergence of 4 mm h^{-1} at the farthest point from the rotation axis, reproducing the relatively constant divergence of the Somalian Plate about the present-day rotation pole south-southwest of Madagascar since at least 20 Ma (Saria et al., 2013, 2014; DeMets and Merkouriev, 2016, 2021; Stamps et al., 2021; Fig. 1a). Given the model duration of 150 min, the total extension is 10 mm at the farthest point from the rotation axis.

In order to localize deformation in our models, we include seeds that follow (parts of) the tectonic plate boundaries that form the main present-day EARS template according to GPS analysis by Saria et al. (2013, 2014) and Stamps et al. (2021) (Figs. 1a, 2a, b, e). These seeds are thin (ø = 4 mm) semi-cylindrical bars of viscous material applied on top of the basal viscous layer, causing the overlying sand layer to be locally thinned and weakened (Fig. 2b). Such seeds have been used in previous modelling studies (e.g. Le Calvez and Vendeville, 2002; Zwaan et al., 2016; Molnar et al., 2019), tend to produce strongly localized rift basins, and are deemed ideal to reproduce the localized style of deformation along pre-existing lithospheric weaknesses in the EARS (e.g. Ring, 2014; Kendall and Lithgow-Bertelloni, 2016). We test five main combinations of seed geometries to explore the effect different lithospheric-weakness arrangements could have had on the evolution of the EARS and to obtain a best-fit model for comparison with the present-day rift system. Note that the seed representing the Western Rift in Model D (Figs. 1

and 2e) has a double diameter of 8 mm to simulate a locally increased weakness in the lithosphere along that part of the EARS and that we do not include the Lwandle Plate (LP in Fig. 1a) due to practical limitations. The summarized results of one further experiment with an alternative rotation pole are presented in the Appendix. Detailed results regarding all models are made publicly available as a GFZ data publication (Zwaan and Schreurs, 2023).

2.2 Model materials

We use a brittle–viscous model layering with a 1.5 cm thick top layer consisting of quartz sand representing a 150 km lithosphere dominated by brittle deformation. This quartz sand (Quarzsand A from Carlo Bernasconi AG; http://www.carloag.ch, last access: 1 July 2023) has a grain size of 60–250 µm and internal friction angles between 31.4–36.1°, with a cohesion value of 9 Pa (Zwaan et al., 2018b) (Table 1). The sand has a constant density of 1560 kg m^{-3} when sieved from ca. 30 cm height (Schmid et al., 2020) and is flattened by a scraper at the end of sieving to ensure a flat initial surface.

The underlying 3 cm thick viscous layer, representing the upper 300 km of the sub-lithospheric mantle, consists of a near-Newtonian mixture of SGM-36 polydimethylsiloxane (PDMS) and corundum sand (F120 Normalkorund braun) from Carlo Bernasconi AG ($\eta =$ ca. $1.5 \cdot 10^5$ Pa s, $n = 1.05$–1.10; Zwaan et al., 2018c). The materials are mixed following a 0.965 : 1.00 weight ratio, and the density of the resulting viscous mixture (ca. 1600 kg m^{-3}) is slightly higher than that of the sand layer. Further material properties are presented in Table 1.

Table 2. Scaling parameters.

		Model	Nature
General parameters	Gravitational acceleration (g)	$9.81\,\mathrm{m\,s^{-2}}$	$9.81\,\mathrm{m\,s^{-2}}$
	Divergence velocity (v)	$1.1 \times 10^{-6}\,\mathrm{m\,s^{-1}}$*	$3.4 \times 10^{-7}\,\mathrm{m\,s^{-1}}$
Brittle layer	Material	Quartz sand	Lithosphere
	Peak internal friction angle (φ)	$36.1°$	$30–38°$
	Thickness (h)	$1.5 \times 10^{-2}\,\mathrm{m}$	$1.5 \times 10^{5}\,\mathrm{m}$
	Density (ρ)	$1560\,\mathrm{kg\,m^{-3}}$	$2800\,\mathrm{kg\,m^{-3}}$
	Cohesion (C)	$9\,\mathrm{Pa}$	$1.5 \times 10^{8}\,\mathrm{Pa}$
Viscous/ductile layer	Material	PDMS–corundum sand mixture	Sub-lithospheric mantle
	Thickness (h)	$3 \times 10^{-2}\,\mathrm{m}$	$3 \times 10^{5}\,\mathrm{m}$
	Density (ρ)	$1600\,\mathrm{kg\,m^{-3}}$	$3300\,\mathrm{kg\,m^{-3}}$
	Viscosity (η)	$1.5 \times 10^{5}\,\mathrm{Pa\,s}$	$1 \times 10^{20}\,\mathrm{Pa\,s}$
Dynamic scaling values	Brittle stress ratio (R_s)	26	27
	Ramberg number (R_m)	85	85

* Maximum divergence velocity, away from the rotation axis.

2.3 Model scaling

We use standard scaling methods to make sure our analogue models adequately represent the natural situation in the EARS (see scaling parameters in Table 2). Since brittle materials have strain-rate-independent rheologies, the angle of internal friction of our quartz sand ($36.1°$) is the main factor for scaling purposes. This value is very similar to values obtained from experimentally deformed rocks ($31–38°$; Byerlee, 1978; Table 2) and is generally considered to be similar for brittle parts of the mantle as well (e.g. Brun, 1999, 2002). We assume a simplified brittle-deformation-dominated lithosphere in our models, which is therefore appropriately represented by our quartz sand.

Scaling viscous materials becomes more intricate than scaling brittle materials due to the strain-rate-dependent rheology of the former. Using the stress ratio between the model and nature (σ^*, convention: $\sigma^* = \sigma_\mathrm{model}/\sigma_\mathrm{nature}$; $\sigma^* = \rho^* \cdot h^* \cdot g^*$, where ρ^*, h^*, and g^* are density, length, and gravity ratios, respectively; Hubbert, 1937; Ramberg, 1981) and the viscosity ratio (η^*), we obtain the strain rate ratio ε^* (Weijermars and Schmeling, 1986): $\dot{\varepsilon}^* = \sigma^*/\eta^*$. With the strain rate ratio we can subsequently compute the velocity and time ratios (v^* and t^*): $\dot{\varepsilon}^* = v^*/h^* = 1/t^*$. Assuming a low viscosity of $1 \times 10^{20}\,\mathrm{Pa\,s}$ for the sub-lithospheric mantle (e.g. Steinberger and Calderwood, 2006), our $4\,\mathrm{mm\,h^{-1}}$ divergence velocity scales up to ca. $1 \times 10^{4}\,\mathrm{mm\,yr^{-1}}$. This velocity is much higher than typical rift divergence rates along the EARS (e.g. Saria et al., 2014; Stamps et al., 2021; Fig. 1), and previous modelling efforts have shown that high extension rates can lead to increased brittle–viscous coupling and distributed extension or "wide rifting" (e.g. Brun, 1999; Zwaan et al., 2016, 2019). However, as long as the seeds localize deformation properly, and no indications of distributed rifting are observed (as is clearly the case in our models), the high divergence velocity in our models can be deemed acceptable for the purpose of our study.

In addition, we consider the dynamic similarity of the model to the natural example through the R_s ratio and the Ramberg number. We derive the dynamic similarity between the brittle sand layer and the natural lithosphere using the R_s ratio between the gravitational stress and the cohesive strength or cohesion C (Ramberg, 1981; Mulugeta, 1988): $R_\mathrm{s} = $ gravitational stress / cohesive strength $= (\rho \cdot g \cdot h)/C$. When assuming a combined cohesion of $100\,\mathrm{MPa}$ for the lithosphere, together with the $9\,\mathrm{Pa}$ cohesion of our quartz sand, we obtain a R_s of 26 for our models and 27 for the natural example. The Ramberg number R_m considers the dynamic similarity scaling of viscous materials (Weijermars and Schmeling, 1986): $R_\mathrm{m} = $ gravitational stress / viscous strength $= (\rho \cdot g \cdot h^2)/(\eta \cdot v)$. It has a value of 85 for both the viscous mixture and the sub-lithospheric mantle in nature, respectively. Since both the R_s and R_m values of our models are quite similar to those in their natural equivalent, we consider our models reasonably well scaled for simulating large-scale continental rifting processes.

2.4 Model monitoring and analysis

We monitor the surface evolution of our models through time-lapse photography by means of a camera set-up consisting of three aligned high-resolution Nikon D810 (36.3 MP) cameras (Zwaan et al., 2021, 2022; Schmid et al., 2022a, b). Top view images from the central camera together with a $4 \times 4\,\mathrm{cm}$ surface grid made of corundum sand (< 1 mm thick) provide first-order insights into model evolution. Additional model surface analysis involves photogrammetry on time-lapse imagery from the other two obliquely oriented cam-

eras. We use Agisoft Photoscan photogrammetry software (http://www.agisoft.com, last access: 1 July 2023) to generate digital elevation models, enabling an assessment of model topography variations over time, notably rift basin evolution, in QGIS (http://www.qgis.org, last access: 1 July 2023). The time-lapse imagery also allows a more detailed analysis and quantification of model surface deformation through means of digital image correlation (DIC) techniques (e.g. Adam et al., 2005; Boutelier et al., 2019; and references therein). This DIC analysis involves the tracing of horizontal displacements on imagery from different time steps (here 10 mm of divergence) using LaVision DaVis 10.2 DIC software. From the horizontal displacement data we derive incremental maximum normal strain maps that serve as a proxy for tracing active extensional deformation in the models over time.

3   Results

3.1   Model A

The results of Model A, with standard diameter seeds ($\emptyset = 4$ mm), tracing most present-day active EARS plate boundaries (see Sect. 2.1), are presented in Fig. 3. Early deformation is not clearly expressed on topography maps when compared to what is revealed in the DIC results (as is the case in all subsequent models as well; Figs. 4–7). The first hints of surface deformation on topography maps appear in the northernmost part of the model after some 20 to 30 min, at the simulated Main Ethiopian Rift–Kenya Rift location (Fig. 3b and c). Subsequently a mostly N–S-oriented through-going rift system develops as rift-related subsidence propagates southward, crossing over into the simulated Malawi Rift. Minor subsidence is visible at the simulated Western Rift as well, segregating the Victoria Plate model equivalent, but there is no trace of deformation along the eastern margin of the simulated Rovuma Plate (Fig. 3).

In contrast to the topography data, the DIC results show that deformation is in fact already localizing during the earliest stages of the model run (Fig. 3g and m). After 10 min, extensional deformation is observed along large parts of the most central seed segments. These structures develop conjugate sets of rift boundary faults, as indicated by the parallel bands of localized deformation, and all structures active in Model A are seen to be deforming by the 20 min mark (Fig. 3h and n), when a moderate degree of deformation is also active along the simulated Western Rift, the effect of which is also nicely visible in the eastward displacement results (Fig. 3m–r). Furthermore, the clear northward increase in eastward displacement seen in the eastern part of the model highlights the clockwise rotational motion applied in our set-up (Fig. 3m–r). Note also the much less expressed gradient on the western side of the model, indicating some minor rotation there as well, which we regard to be a boundary effect (Fig. 3m–r).

Some additional important details are revealed by the DIC results. Firstly, we find that the southward propagation of active deformation is indeed largely completed after some 20 min, but it continues at a slow rate until the end of the model run (Fig. 3g–l). Furthermore, towards the end of the model run, the most advanced rift basins in the model (the simulated Kenya and Malawi rifts) seem to develop a central band of extensional deformation in addition to the active rift boundary faults (Fig. 3l).

3.2   Model B

Model B has the same standard seed diameter as Model A ($\emptyset = 4$ mm), but the seeds trace less of the present-day EARS plate boundaries (Fig. 4). A major difference with Model A is that in Model B, the simulated Western Rift is much better developed, and there is only a minor connection between the simulated Kenya Rift and the Malawi Rift, whereas Model A features a clear through-going rift basin (Figs. 3, 4).

The DIC results provide important additional details (Fig. 4g–r). As in Model A, deformation already localizes in the early stages, before it becomes visible at the model surface. We also observe that most structures are already activated around $t = 20$ min. The main differences with Model A are related to the increased development of the simulated Western Rift, as highlighted by the eastward displacement analysis (Fig. 4m–r). This analysis shows the same general rotation imposed along the eastern bound of the model, but the development of the simulated Western Rift causes the presence of the Victoria Plate model equivalent, which undergoes an independent anticlockwise rotation (as indicated by the decreasing eastward displacement towards the north; Fig. 4m–r).

Further important details are similar to Model A in that we observe a relatively fast early southward propagation of active rifting followed by a slow propagation during the rest of the model run (Fig. 3g–l), as well as intra-rift deformation along the most developed rift basin (the simulated Kenya Rift; Fig. 3l). An additional observation from DIC data is that the simulated Western Rift initiates its development in the south and gradually propagates northward, eventually deflecting northward (Fig. 4g–l). Finally, both the topography and DIC data show that the link between the simulated Western and Malawi rifts (i.e. the Rukwa Rift model equivalent), which is 45° oblique to the model axis, is rather narrow compared to those rift segments that are more parallel to the model axis (Fig. 4a–l).

3.3   Model C

Model C is a rerun of Model B, with a slightly reduced seed length in both the simulated Kenya and Western rifts so that the seeds do not laterally overlap (similar to the models from Zwaan et al., 2020; Figs. 1d, 4a, 5a). This reduced seed length in Model C mitigates the topographical impact
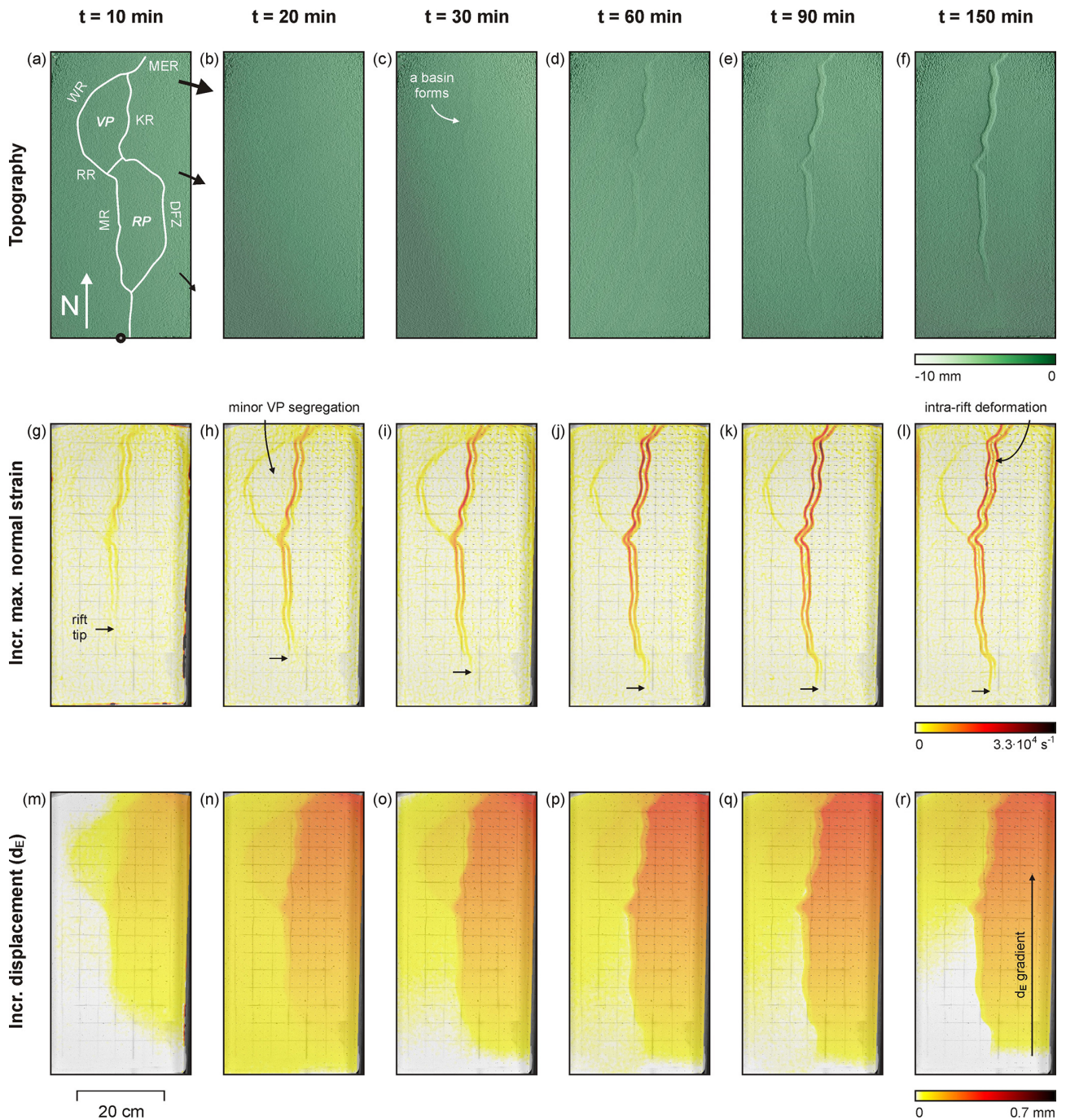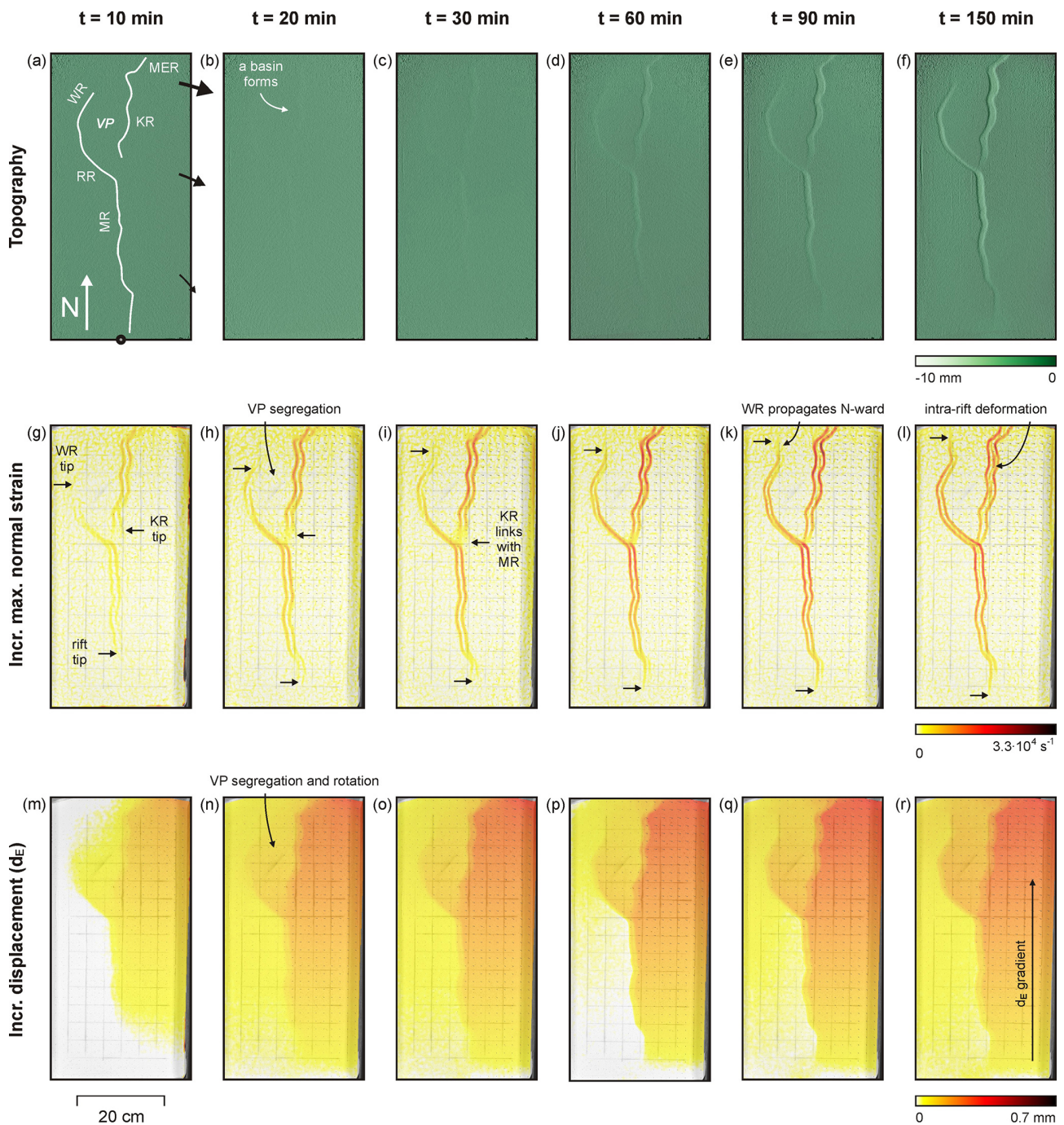
Figure 3. Results of Model A, shown in map view. **(a–f)** Topography evolution. The initial seed geometry is indicated in panel **(a)**. Lighting is applied from the left. **(g–l)** Incremental maximum normal strain **(m–r)**. Incremental eastward displacement (d_E). Increments for digital image correlation (DIC) analysis: 10 min of divergence. DFZ: Davie Fracture Zone; KR: Kenya Rift; MER: Main Ethiopian Rift; MR: Malawi Rift; RP: Rovuma Plate; RR: Rukwa Rift; VP: Victoria Plate; WR: Western Rift.

of the simulated Kenya and Western rifts, even though DIC results show (distributed) extension past the rift tips (Figs. 4f, l, 5f, l). Note that the simulated Western Rift does not deflect as far northward as in Model B but does generally propagate northward along the trace of the seed, and as a result of

its activity the anticlockwise-rotating Victoria model equivalent is established (Figs. 4g–r, 5g–r). Parallel to its Western Rift model equivalent, the simulated Kenya Rift propagates southward, but the southern rift tip ends in a diffuse deformation zone (Fig. 5g–l). Similar to Models A and B, over-
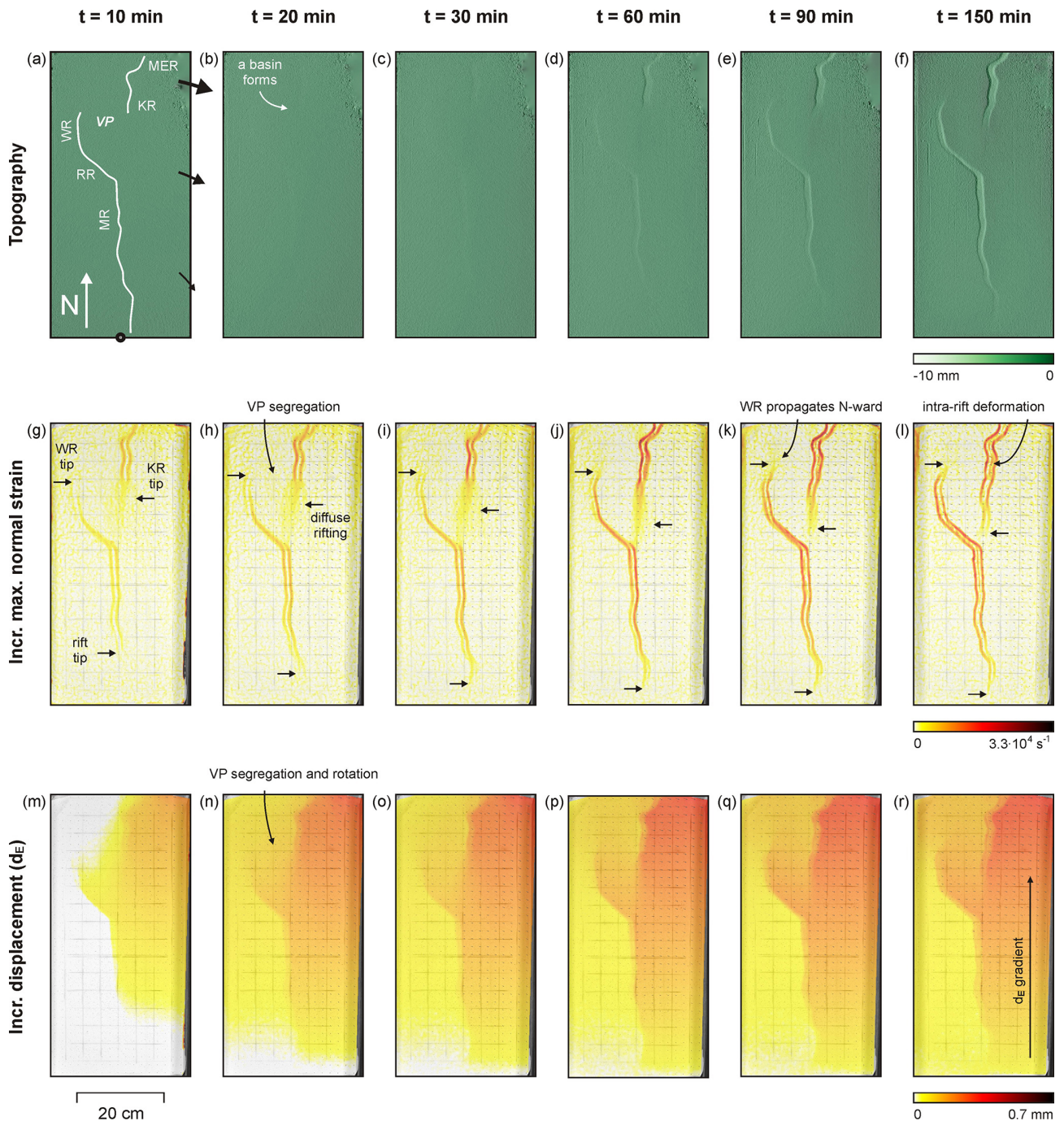
Figure 4. Results of Model B, shown in map view. **(a–f)** Topography evolution. The initial seed geometry is indicated in panel **(a)**. Lighting is applied from the left. **(g–l)** Incremental maximum normal strain **(m–r)**. Incremental eastward displacement (d_E). Increments for digital image correlation (DIC) analysis: 10 min of divergence. KR: Kenya Rift; MER: Main Ethiopian Rift; MR: Malawi Rift; RR: Rukwa Rift; VP: Victoria Plate; WR: Western Rift.

all southward propagation of extension is observed, decelerating after 20 min but never fully halting (Figs. 3g–l, 4g–l, 5g–l), and intra-rift deformation localizes along the axes of the most developed rift segments (Kenya and Malawi rifts; Fig. 5l). Furthermore, as seen in Model B, the ca. 45° oblique

(NW–SE) simulated Rukwa Rift is rather narrow compared to other, less obliquely oriented rift segments (Figs. 4f and l, 5f and l).

Figure 5. Results of Model C, shown in map view. **(a–f)** Topography evolution. The initial seed geometry is indicated in panel **(a)**. Lighting is applied from the left. **(g–l)** Incremental maximum normal strain **(m–r)**. Incremental eastward displacement (d_E). Increments for digital image correlation (DIC) analysis: 10 min of divergence. KR: Kenya Rift; MER: Main Ethiopian Rift; MR: Malawi Rift; RR: Rukwa Rift; WR: Western Rift.

3.4   Model D

Model D is a rerun of Model A, with a double-diameter seed (ø = 8 mm) tracing the Western Rift (Figs. 2e, 3, 6). In contrast to Model A, however, the dominant rift branch in the north of the model is the simulated Western Rift (in-

stead of the Kenya Rift) (Figs. 3f and l, 6f and l). Hence, we obtain a largely westwardly curved rift system in the north of Model D, with only minor deformation at the simulated Kenya Rift (Fig. 6f and l) and a very faint reactivation of the eastern borders of the simulated Rovuma Plate
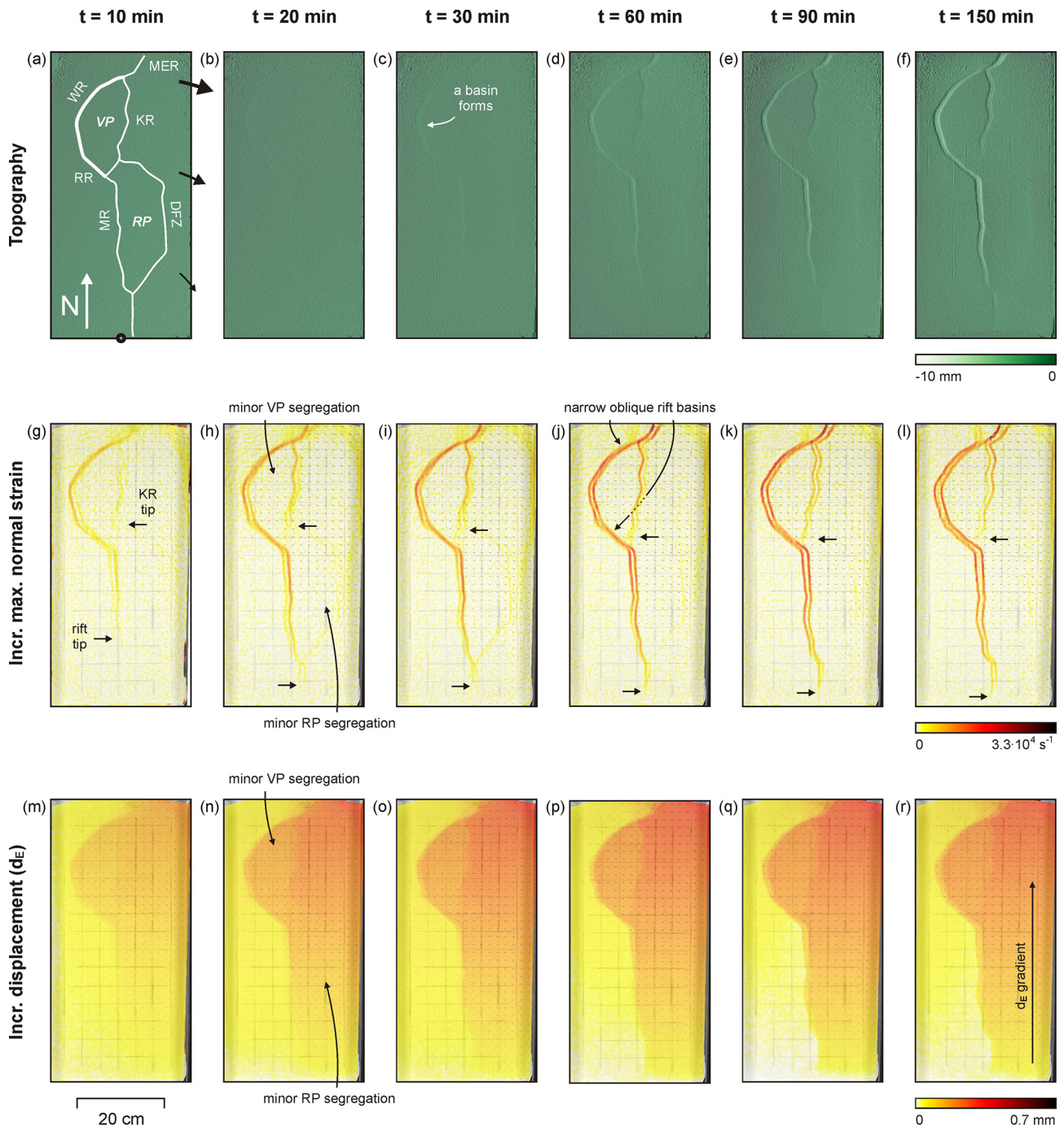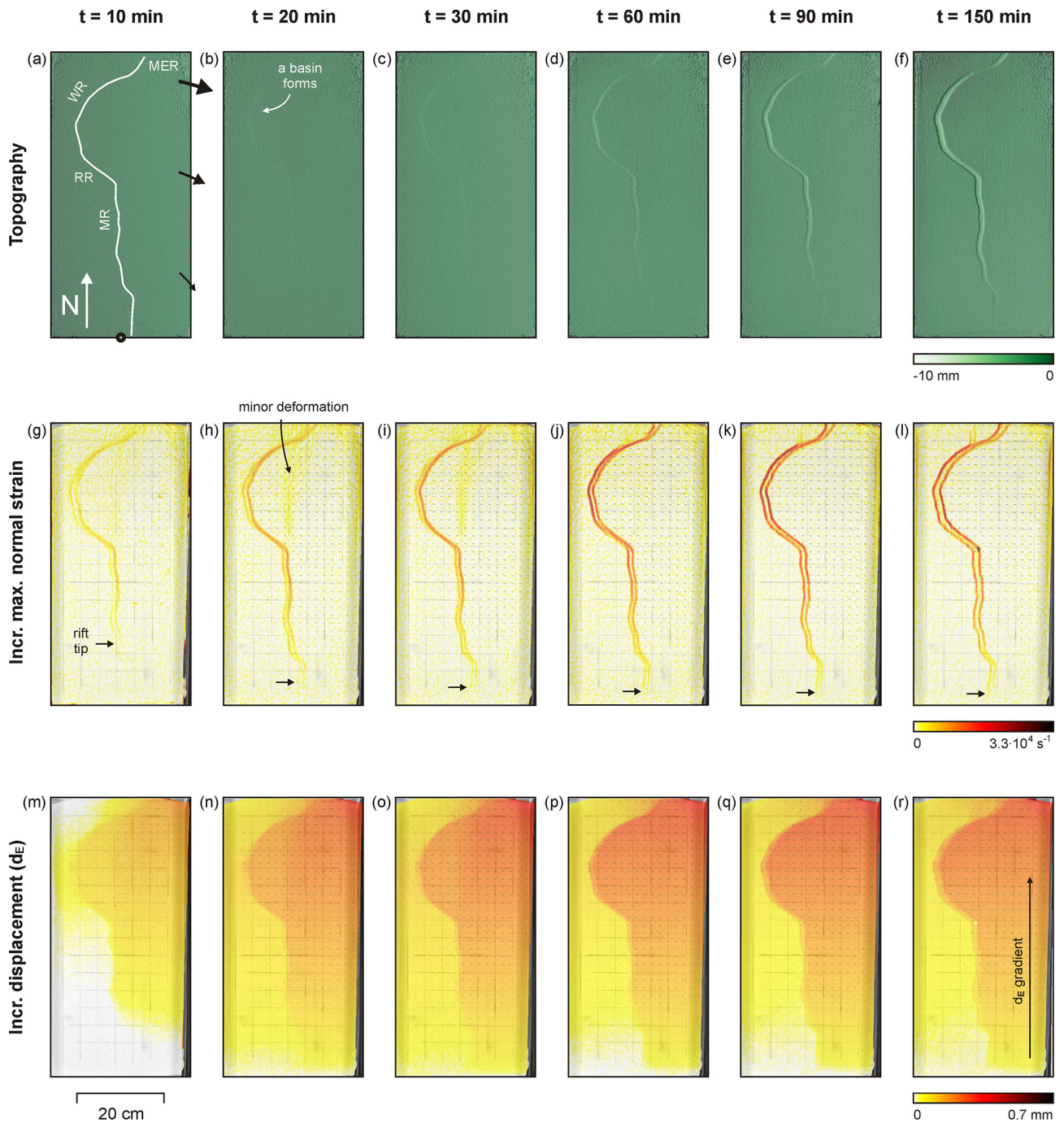
Figure 6. Results of Model D, shown in map view. **(a–f)** Topography evolution. The initial seed geometry is indicated in panel **(a)**, where the Western Rift seed had a double diameter (ø = 8 mm). Lighting is applied from the left. **(g–l)** Incremental maximum normal strain **(m–r)**. Incremental eastward displacement (d_E). Increments for digital image correlation (DIC) analysis: 10 min of divergence. DFZ: Davie Fracture Zone; KR: Kenya Rift; MER: Main Ethiopian Rift; MR: Malawi Rift; RP: Rovuma Plate; RR: Rukwa Rift; VP: Victoria Plate; WR: Western Rift.

since initiation of the model run (Fig. 6g–l). As a result of this configuration, all domains east of the dominant Western Rift model equivalent move eastward, where the simulated Kenya Rift slightly mitigates this effect so that a gen-

erally eastward-moving Victoria Plate model equivalent can be observed, which moves a bit slower than the eastern-most domain (Fig. 6m–r). Note that in contrast to Models B and C, this microplate does not rotate significantly,

Figure 7. Results of Model E, shown in map view. **(a–f)** Topography evolution. The initial seed geometry is indicated in panel **(a)**. Lighting is applied from the left. **(g–l)** Incremental maximum normal strain **(m–r)**. Incremental eastward displacement (d_E). Increments for digital image correlation (DIC) analysis: 10 min of divergence. MER: Main Ethiopian Rift; MR: Malawi Rift; RR: Rukwa Rift; WR: Western Rift.

as indicated by the lack of a clear north–south displacement gradient (Figs. 4m–r, 5m–r, 6m–r). Also the Rovuma Plate model equivalent in Model D exhibits a faintly different eastward motion compared to the general easternmost domain (Fig. 6m–o).

In Model D we also observe that the general southward propagation of extension is strongly decelerating after 20 min, but no northward propagation is seen in the simulated Western Rift (Fig. 6g–l). Furthermore, not only is the oblique Rukwa Rift segment between the simulated Western Rift and Malawi Rift narrower in shape than the ca. N–S-oriented rift

basins, this is also true of the highly oblique link between the simulated Western Rift and Main Ethiopian Rift in the north (Fig. 6f and l). Finally, although it is not that clearly visible in the images, there are some hints of intra-rift deformation in the simulated Malawi Rift, Western Rift, and Main Ethiopian Rift (Fig. 6l).

3.5 Model E

In Model E, we apply a seed with a standard diameter ($\emptyset = 4$ mm) that follows the westernmost limits of the EARS only (Fig. 7a). The results are very similar to those of Model D, even though the seed geometry is quite different (Figs. 6 and 7). We observe the development of a rift system along the whole length of the seed in Model E, following the various curves of said seed. After 20 to 30 min the earliest structures become visible at the surface (Fig. 7b and c), whereas DIC analysis shows early extension along most of the seed, which propagates southward until the 20 min mark, before slowing down drastically (Fig. 7g–l). Similar to the structures in Model D, the oblique parts of the rift system are narrower, and all domains east of the rift system move eastward, as shown by the north–south displacement gradient (Fig. 7f, l, m–r). Furthermore, the DIC results also show some localization of extension along the axis of the model during the first 30 min of model development (Fig. 7g–i).

4 Discussion

4.1 Synopsis and comparison to previous modelling studies

In Fig. 8 we present a summary overview of our model results, taken at the end of each model run, which forms the basis for a synopsis of model results and comparison to previous modelling studies presented in the following sections.

4.1.1 Rotational rifting

The first important insight from our model results is that the rotational divergence boundary condition leads to an overall northwardly increase in divergence velocity, and thus in extension rates, which correlates with the most developed rift basins occurring in the northern part of the models (Figs. 3–8). This correlation has been observed in many previous modelling studies involving rotational divergence (e.g. Souriot and Brun, 1992; Benes and Scott, 1996; Sun et al., 2009; Molnar et al., 2017, 2018; Mondy et al., 2018; Khalil et al., 2020; Zwaan and Schreurs, 2020; Zwaan et al., 2020; Schmid, et al., 2022a, b).

A further observation related to rotational divergence in our models is the initial fast rift propagation of extension towards the rotation axis in the south, followed by a deceleration and a slow propagation in the later stages of the model run. This effect was previously reported by Schmid

et al. (2022a, b) and upon closer inspection is also visible in the models by Mondy et al. (2018), Maestrelli et al. (2020), and Zwaan et al. (2020). Indeed, this fast propagation of extension is not directly obvious from surface imagery or topography data and requires DIC results to be revealed, highlighting the need for such DIC analysis to monitor source deformation in analogue models. It also shows that rift propagation in the models is in fact a much faster process than perhaps previously interpreted from surface imagery and topography data: very early on in the evolution of the models, rifting started along most of the rift system, establishing the template for its subsequent structural evolution.

4.1.2 Seed geometry and microplates

Rotational divergence itself would be expected to produce a linear rift system along the axis of the model (e.g. Martin, 1984; Benes and Scott, 1996; Mondy et al., 2018; Zwaan et al., 2020; Schmid et al., 2022a, b), but the structural inheritance applied in our models forces the model to deviate from this template, generating a range of rift basin arrangements. When comparing the various seed geometries we applied to the final structures produced in the models, the relations are somewhat complex (Fig. 8). In Model A, representing the end-member with the dominant rift structures situated farthest to the east, not all seeds are reactivated (Figs. 3, 8a–d). It seems that extension preferentially localized in the north of the model, along the simulated Main Ethiopian Rift and Kenya Rift, where the largest degree of extension is applied, before swiftly propagating south along the strike of the model, mostly avoiding the seeds tracing the Western Rift and the eastern margin of the Rovuma Plate (Fig. 3g–l). We also found some localization of deformation along the model axis in Model E (Fig. 7g–i). It may very well be that this orientation of rifting (i.e. near the axis of the system) is ideal in this type of model so that the seeds that are aligned accordingly are preferentially activated at the expense of those that are off-centre, in this case the Western Rift and eastern margin of the Rovuma Plate. Such preferential reactivation of more favourably oriented weaknesses has been observed in various previous modelling studies (e.g. Henza et al., 2010, 2011; Zwaan and Schreurs, 2017; Molnar et al., 2019, 2020; Maestrelli et al., 2020; Wang et al., 2021; Zwaan et al., 2021, 2022; Bonini et al., 2023).

However, when these seeds are not fully linked up as in Models B and C, deformation is forced to follow the offset seeds, resulting in a rift pass or overlap configuration (Nelson et al., 1992; Hieronymus, 2004; Kolawole et al., 2021a; Figs. 4, 5, 8e–l). The overlapping configuration of these rifts, where one rift becomes gradually dominant over the other along-strike, causes the separate rotation of the central rift pass area (in this case the simulated Victoria Plate; Figs. 4m–r, 5m–r, 8h and l). Such rotation of rift pass blocks has been reported in numerous modelling studies (e.g. Oldenburg and Brune, 1975; Katz et al., 2005; Tentler and Acocella, 2010;
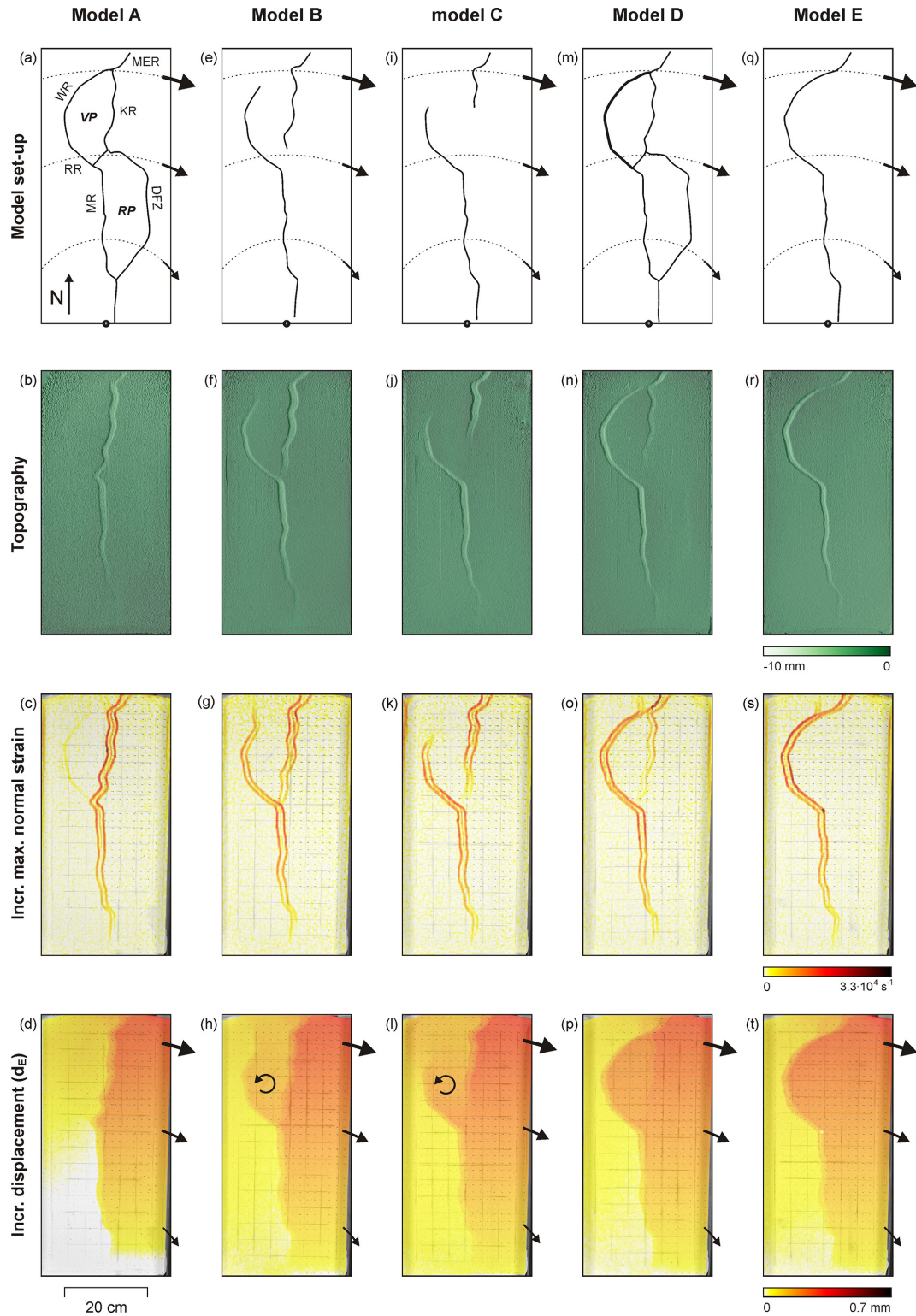
Figure 8. Overview of final stage ($t = 150$ min) model results from Models A–E, shown in map view. **(a–e)** General model set-up detailing seed geometries and model kinematics. **(f–j)** Final model topography. **(k–o)** Incremental maximum normal strain. **(p–t)** Incremental eastward displacement (d_E). Increments for digital image correlation (DIC) analysis: 10 min of divergence. DFZ: Davie Fracture Zone; KR: Kenya Rift; MER: Main Ethiopian Rift; MR: Malawi Rift; RR: Rukwa Rift; RP: Rovuma Plate; VP: Victoria Plate; WR: Western Rift.

Zwaan et al., 2016, 2018a, 2020; Brune et al., 2017; Molnar et al., 2017, 2018; Glerum et al., 2020; Neuharth et al., 2021). Important in these systems is that both overlapping rifts propagate in opposite directions as the block rotates, which is also seen in our Models B and C (Figs. 4m–r, 5m–r). In combination with regional-scale rotation, this means that active extension (i.e. rift basins) can propagate both (regionally) towards and (locally) away from the rotation pole, as proposed by Zwaan and Schreurs (2020) (Figs. 1d, 4g–l, 5g–l).

Model D (Fig. 8m–p) continues the westward shift in rift localization shown in Models B and C (Fig. 8e–l). This more westward concentration of rifting is due to the thicker seed tracing the Western Rift, which overrides the tendency of the model to preferentially localize deformation along the central model axis that is shown in Models A and E (Figs. 7g–l, 8). A thicker seed represents a more impactful weakness in the system, and such weaknesses naturally attract more deformation, as also observed in previous modelling studies (e.g. Henza et al., 2010, 2011; Wang et al., 2021; Zwaan et al., 2021; Osagiede et al., 2021). Even so, the Kenya Rift seed still localizes part of the deformation in the system, creating a Victoria Plate model equivalent as in Models B and C, but with the crucial difference that this plate does not rotate anticlockwise (Figs. 6m–r, 8p). Instead, in Model D it merely moves along with the rotation of the eastern domain, albeit at a slower rate due to the presence of the simulated Kenya Rift (Fig. 6m–r). In contrast to Model A, the eastern edge of the Rovuma Plate did slightly activate in Model D, despite the same unfavourable arrangement with respect to the overall tectonic set-up (Figs. 3, 6, 8a–d, 8m–p).

Model E is the other end-member model, where the single seed localizes deformation along the Western Rift and Malawi Rift traces (Figs. 7, 8q–t). Even though no seed was present along the Kenya Rift trace, there are some hints of minor early extension localization there, highlighting the model's preference to localize deformation along its central axis (Fig. 7g–j). Nevertheless, the experiment results in a solid eastern domain that rotates eastward in a clockwise orientation (Figs. 7g–l, 8t), without any hint of the Victoria microplate.

4.1.3 Additional observations: intra-rift deformation and oblique rifts

In addition to the large-scale observations discussed above, some more detailed insights can be gained from our models. Firstly, the DIC analysis shows the initial localization of boundary faults flanking the rift segments, followed by intra-rift deformation along the central axis of the most developed rift basins (Fig. 8c, g, k, o, s). This shift in deformation has been observed in DIC results of previous models as well (Schmid et al., 2022a, b) and can be explained by the rise in the viscous layer below the rift axis in this type of brittle–viscous models (e.g. Zwaan et al., 2016, 2018a, 2020), while

the rift boundary faults have already accommodated most of their slip at that point in time.

The various orientations of the rift segments provide some final insights. Indeed, in places where the rift basins are oriented obliquely with respect to the model axis (and to the general extension direction), they are much narrower than those rift basins that are parallel to the model axis (Fig. 8b, f, j, n, r). This is a straightforward effect of the local oblique extension direction: the larger the extension obliquity, the more the system moves towards steep strike-slip faulting (e.g. Corti et al., 2007; Zwaan et al., 2016). Here it must be noted that for an exact determination of the extension obliquity, the rotational divergence and the associated curved displacement traces need to be taken into account (Fig. 8a, e, i, m, q; Smith, 1993), but the general orientation of the rifts with respect to the model axis provides a first-order indication that is sufficiently accurate (see also the Appendix).

A detail that is however not captured in our models concerns offset en echelon structures, which are typical of oblique extension models (e.g. Withjack and Jamison, 1986; Tron and Brun, 1991; Bonini et al., 1997; Keep and McClay, 1997; Zwaan et al., 2021, 2022). The simulated Western Rift should especially be expected to contain various offset subbasins, as shown by previous models (which, however, do not incorporate rift propagation; Corti et al., 2007). This is likely due to the relatively thin sand layer in our model's set-up, as well as the general brittle–viscous set-up with seeds preventing the development of such details (compare our results with Figs. 5 and 7 in Zwaan and Schreurs, 2017). As such, our models are best suited to reveal the large-scale trends in such settings.

4.2 General model limitations

Before comparing our model results with the EARS, it is important to point out some general limitations of our models. Firstly, as mentioned in Sect. 4.1.3, our models should be used for interpreting the evolution of large-scale tectonic structures as we apply a highly simplified, brittle-deformation-dominated lithosphere. Furthermore, the modelling of rotational divergence on a sphere (as is the case in nature) is done on a flat plane (Zwaan et al., 2020), which may cause some distortions towards the rotation pole and affect the rate of rift propagation in our models (Schmid et al., 2022a, b). Yet these minor distortions are not considered to significantly undermine our model results. Some boundary effects occur along the long edges of our model, as shown by the slight rotation of the westernmost domain in our models, but also the impact of these boundary effects on the large-scale evolution of the model are minor. Another limitation is the lack of surface processes (erosion and sedimentation) in our models, which are known to affect rift evolution (e.g. Burov and Cloetingh, 1997; Buiter et al., 2009; Neuharth et al., 2022). However, the analogue models by Zwaan et al. (2018a) suggest that surface processes do not significantly

alter the large-scale structures of young continental rift systems, and as such, our model results remain applicable on a first-order scale. Finally, we apply far-field tectonic rotation of the Somalian Plate in our models with deformation driven by sidewall motion (Fig. 2), thus ignoring the gravitational energy potential or mantle flow that may be largely driving EARS development in nature (e.g. Bagley and Nyblade, 2013; Kendall and Lithgow-Bertelloni, 2016; Rajaonarison et al., 2021, 2023). Nevertheless, our models still provide valuable insights into the links between Somalian Plate rotation and the evolution of the EARS, even if this rotation would be a consequence rather than the primary driver of EARS development.

4.3　Comparison to the EARS

4.3.1　Southward rift propagation along the EARS

Of the five rifting models completed for this study, Model C provides the best fit with the present-day tectonic setting in the EARS (Fig. 9a–c), and we can use the model as a basis to discuss the evolution of the natural example. First of all, we can infer a general southward propagation of rift basin development along the whole length of the EARS, as previously proposed by Zwaan and Schreurs (2020), due to the rigid clockwise rotation of the Somalian Plate (e.g. Saria et al., 2014; Stamps et al., 2021; Figs. 1a, 9a). This southward propagation is in line with data from the EARS, suggesting a southward younging direction of rifting (Chorowicz, 2005; Macgregor, 2015). Importantly, our models also suggest that deformation may already have rapidly propagated over large parts of the system during the earlier phases of EARS development, which is a logical result of rigid plate rotation causing rotational deformation along the whole length of the EARS. Such a fast southward propagation of EARS structures over the last 20 Myr is inferred by Macgregor (2015) and Purcell (2018) (Fig. 9d–f).

We must however point out that the exact age of the various rift basins along the EARS is debated (Purcell, 2018; Zwaan and Schreurs, 2020; Michon et al., 2022; Martin, 2023; and references therein), and such early extension may have occurred without leaving behind clear field evidence due to the initially limited amount of extension. Moreover, studies have shown variations in lithospheric thickness and strength along the EARS (e.g. Globig et al., 2016; Daly et al., 2020), which can have halted or promoted rift development (e.g. Benes and Scott, 1996; Brune et al., 2017). This influence of lithospheric thickness and strength on rift development is to a degree also illustrated by the delayed southward propagation of the simulated Kenya Rift when a shorter seed is included in our models (compare Models B and C in Fig. 8). A further complication in this context is the magma-rich nature of the EARS, which may cause magmatic underplating or strongly localize rift deformation (magma-assisted rifting; Buck, 2004, 2006) so that rift basins may develop

faster than in magma-poor settings, skewing the tectonic signal. Such magmatism also provides concrete time constraints on rift initiation (e.g. Ayalew et al., 2006; Wolfenden et al., 2005; Michon et al., 2022), but these records may not always be fully preserved in the sub-aerial conditions of the EARS, as may be the case for any syn-rift sediments as well. It is thus clear that continued research is required to improve our understanding of the large-scale evolution of the EARS. Still, our model results suggest that rigid rotational motion of the Somalian Plate rotation can readily explain the general southward propagation of rifting, as proposed by Chorowicz (2005) and shown on maps by Macgregor (2015) and Purcell (2018) (Fig. 9d–f).

4.3.2　Microplates within the EARS

A further key observation in our best-fit Model C concerns the evolution of microplates. The simulated Victoria Plate segregated and started rotating anticlockwise early on during the model run, as a necessary result of the rapid nucleation of the overlapping Western Rift and Kenya Rift model equivalents (Figs. 5m–r, 8l). The same rift pass mechanism is indeed clearly active in the EARS (Glerum et al., 2020; Zwaan and Schreurs, 2020), where GPS observations demonstrate the ongoing rotation of the Victoria Plate (Saria et al., 2014; Stamps et al., 2021) (Figs. 1a, 9a). From our Model C results, we can propose that the Victoria Plate has been established and rotating ever since the development of the Western and Kenya Rift started around 12 Ma (Fig. 9d) and should have been in full swing by 5 Ma, when both rifts were well established (Fig. 9e) (Macgregor, 2015). Similar to our models, we should then also expect the Western Rift to have propagated northward since its inception, and the Kenya Rift should have propagated southward (all while the rift system as a whole was propagating southward; see Sect. 4.3.1), which is in general agreement with observations from the EARS (Macgregor, 2015; Purcell, 2018; Martin, 2023). During (the early stages of) our Model C run, the southern tip of the simulated Kenya Rift also exhibits the diffuse style of deformation observed in nature (Figs. 1b, 5g–l).

In contrast to the Victoria Plate, the Rovuma Plate is not clearly represented in Model C (although the Rovuma Plate is slightly developed in Model D; Fig. 6). The Rovuma Plate is situated close to the rotation pole and does involve very minor ($< 1\ \mathrm{mm\ yr^{-1}}$), but constant motion along its eastern border (Saria et al., 2014; Stamps et al., 2021; Figs. 1a, 9a), and as such, its rotation is controlled by the more pronounced divergence along the Malawi Rift. Yet, a complete model of the EARS will need to incorporate the evolution of the Rovuma Plate as well, since it does take up about 30 % of the plate divergence in the southern part of the EARS (Saria et al., 2014; Stamps et al., 2021; Figs. 1a, 9a). Similarly, the limited motion of the elusive Lwandle Plate southeast of the Rovuma Plate, which is not included in this study due to practical limitations, needs to be addressed too (Fig. 1a). In fact, it ap-
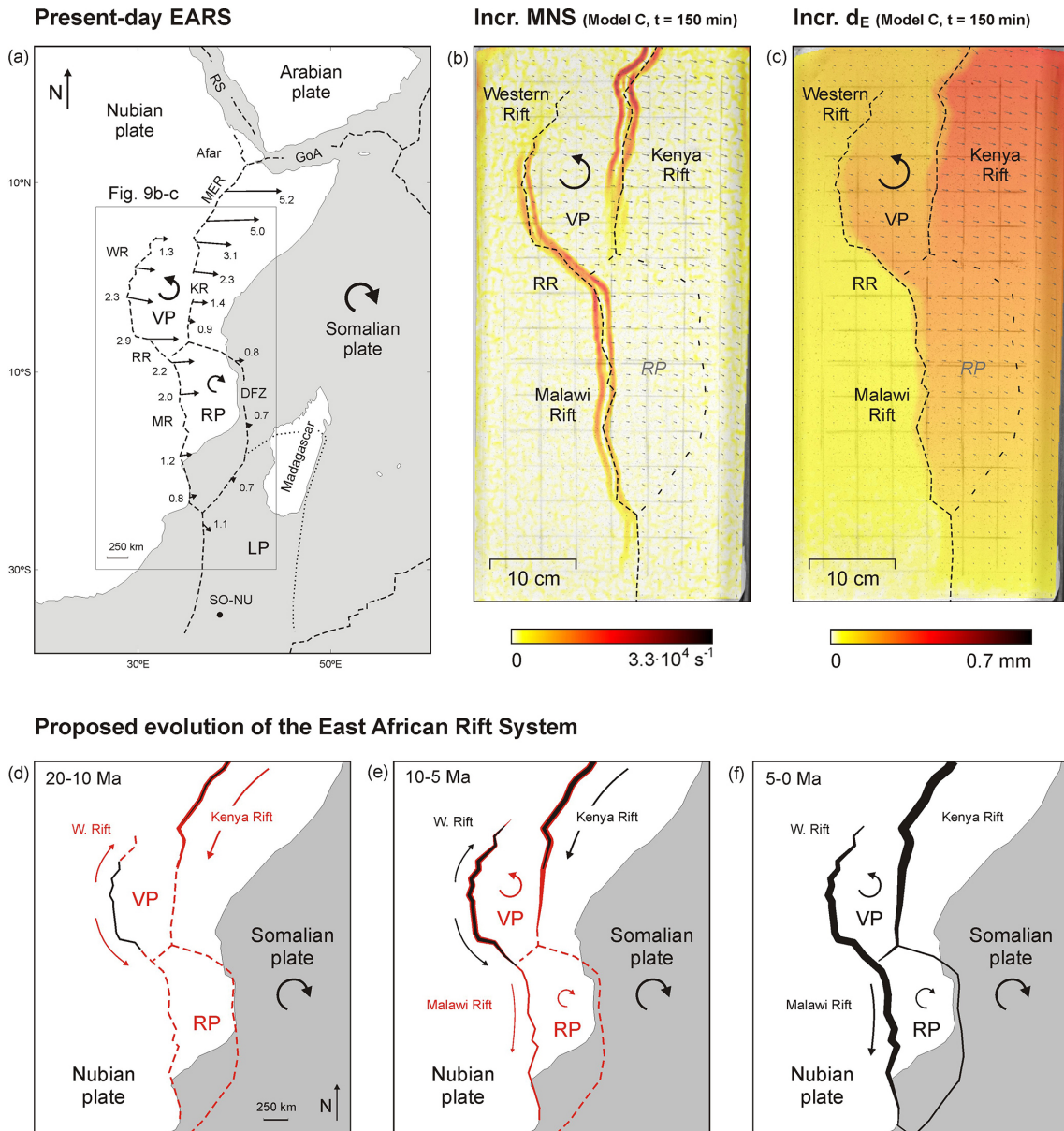
Figure 9. Application of our model results. **(a–c)** Comparison between the East African Rift System (EARS) and our Model C results. **(a)** Tectonic map of the EARS. Plate motions (mm yr^{-1}); dotted lines indicate plate boundaries. Modified after Saria et al. (2013, 2014) and Stamps et al. (2021). **(b)** Incremental maximum normal strain (MNS) localization, which follows the general trace of the EARS, and **(c)** incremental eastward displacement (d_E), which mimics the large-scale plate divergence pattern of the EARS, at the end of the model run. **(d–f)** Proposed evolution of the EARS based on Model C (and D), involving rapid southward propagation of rift-related extension (red), followed by development of discrete rift basins (black). Image modified after Macgregor (2015), Purcell (2018), and Zwaan and Schreurs (2020). DFZ: Davie Fracture Zone; GoA: Gulf of Aden; KR: Kenya Rift; LP: Lwandle Plate; MER: Main Ethiopian Rift; MR: Malawi Rift; RP: Rovuma Plate; RR: Rukwa Rift; RS: Red Sea; SO–NU: Somalia–Nubia rotation pole; WR: Western Rift.

pears that there is no consensus regarding the actual extent of the EARS (Michon et al., 2022), and there may be other rift branches and microplates that have to be considered (Daly et al., 2020; Kolawole et al., 2021a, b; Stamps et al., 2021; Martin, 2023; Wedmore et al. 2023). What can however be predicted from our models is that the Rovuma Plate, similar to the Victoria Plate, could have been segregated at an early

stage of EARS development as extension rapidly propagated southward (Figs. 9d–f). We refrain from making such predictions regarding the Lwandle Plate given its position near the present-day Somalia–Nubia rotation pole (Fig. 1a).

4.3.3   Intra-rift deformation and oblique rifts in the EARS

Two further details observed in our models are also relevant to our interpretation of the EARS. The first is the localization of intra-rift extension along the central axis of the most evolved rift basins (Fig. 8c, g, k, o, s). Such localization is also observed in the Main Ethiopian Rift, which represents the most evolved part of the EARS, apart from the Afar Triangle (Fig. 1a). Here, the so-called magmatic segments belonging to the Wonji Fault Belt are situated along the rift axis and are found to accommodate a significant portion of the total extension in the system as it is nearing breakup (e.g. Ebinger, 2005; Pizzi et al., 2006; Ebinger et al., 2008). It must however be pointed out that our models do not directly simulate the magmatic processes that may promote weakening of the crust in the MER (Buck, 2004, 2006). Yet, basin-inward migration is a well-known phenomenon in other (magma-poor) rift basins as well (e.g. Cowie et al., 2005; Sutra et al., 2013). The second observation concerns the impact of rift orientation on rift structures. Although our models do not provide detailed insights into fault structures, the general oblique/strike-slip nature of the obliquely oriented rift segments such as the Rukwa Rift is clearly recognized (Corti et al., 2007; Morley, 2010; Glerum et al., 2020; Figs. 8d, h, f, p, t, 9b and c).

5   Conclusion

In this study we present a new series of analogue rotational-rifting models specifically tailored to explore the dynamic evolution of the East African Rift System (EARS) and its link to the rotation of the Somalian Plate. Our model results lead us to the following conclusions:

- Rotational rifting leads to rift propagation in all our model runs. Yet we need to distinguish between the propagation of rift-related deformation, which can move very rapidly towards the rotation axis, and the surface expression of this rapidly propagating deformation in the shape of discrete rift basins, which can significantly lag behind. We speculate that such rapid propagation towards the Somalia–Nubia rotation pole to the south may have taken place in the EARS as well.

- The different structural-weakness geometries we tested in our models lead to a variety of rift system arrangements, of which our Model C provides the best fit with the EARS. It is clear from our models that laterally overlapping weaknesses are required for the formation of parallel rift basins and the creation of rift pass structures, possibly leading to the segregation of microplates. These plates can start rotating if the rift basins on both sides are sufficiently developed, as is the case for the Victoria Plate in the EARS. Importantly, this involves

the northward propagation of the Western Rift, which goes against the general southward propagation direction of the EARS.

- Additional model observations involve the development of early pairs of rift-bounding faults flanking the rift basins, followed by the localization of deformation along the axes of the most developed parts of the rift system. Such a shift in deformation towards the centre of the rift has been observed along the Main Ethiopian Rift, where it is associated with incipient (magma-rich) continental break-up, but it is also observed in many other rift basins around the globe.

- Finally, we observe how the orientation of rift segments with respect to the regional (rotational) plate divergence affects deformation along these segments. Compared to rift segments that are oriented (near-)perpendicular to the plate divergence direction, obliquely oriented rift segments are less wide and show a component of strike-slip deformation (i.e. oblique extension).

- Overall, we find that our model results generally fit the present-day large-scale features and ongoing deformation along the EARS and have implications for general rift development, rift basin propagation, and the segregation and rotation of microplates.

Appendix A

The five models presented in the main text all have a minor error in that the location of the rotation axis is in fact somewhat too far to the west (Fig. A1). Although this error does somewhat modify the relative direction of plate divergence along the seeds (Fig. A1a and b), the final results in both Model A and Model F with the correct rotation axis location are very similar (Fig. A1). Hence, we conclude that the results from our Models A–E as presented in this paper remain valid.
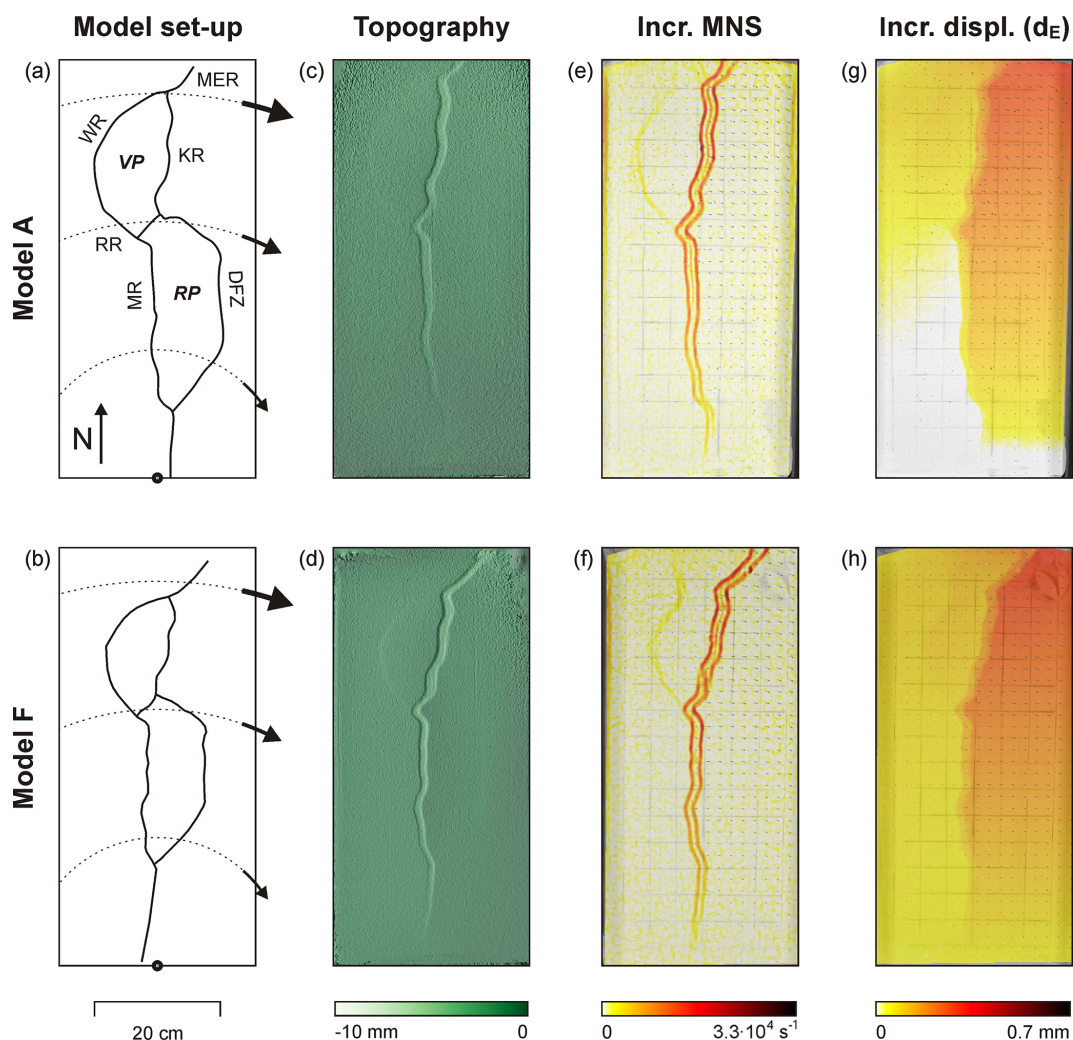
Figure A1. Comparison of final stage ($t = 150$ min) model results from Models A and F. **(a, b)** General model set-up showing seed geometries and model kinematics. **(c, d)** Final model topography. **(e, f)** Incremental maximum normal strain (MNS). **(g, h)** Incremental eastward displacement (d_E). Increments for digital image correlation (DIC) analysis: 10 min of divergence. DFZ: Davie Fracture Zone; KR: Kenya Rift; MER: Main Ethiopian Rift; MR: Malawi Rift; RP: Rovuma Plate; RR: Rukwa Rift; VP: Victoria Plate; WR: Western Rift.

References

Adam, J., Urai, J. L., Wieneke, B., Oncken, O., Pfeiffer, K., Kukowski, N., Lohrmann, J., Hoth, S., Van der Zee, W., and Schmatz, J.: Shear localisation and strain distribution during tectonic faulting – new insights from granular-flow experiments and high-resolution optical image correlation techniques, J. Struct. Geol., 27, 283–301, https://doi.org/10.1016/j.jsg.2004.08.008, 2005.

Ayalew, D., Ebinger, C., Bourdon, E., Wolfenden, E., Yirgu, G., and Grassineau, N.: Temporal compositional variation of syn-rift rhyolites along the western margin of the southern Red Sea and northern Main Ethiopian Rift, Geol. Soc. Spec. Publ., 259, 121–130, https://doi.org/10.1144/GSL.SP.2006.259.01.10, 2006.

Bagley, B. and Nyblade, A. A.: Seismic anisotropy in eastern Africa, mantle flow, and the African superplume, Geophys. Res. Lett., 40, 1500–1505, https://doi.org/10.1002/grl.50315, 2013.

Benes, V. and Scott, S. D.: Oblique rifting in the Havre Trough and its propagation into the continental margin of New Zealand: Comparison with analogue experiments, Mar. Geophys. Res., 18, 189–201, https://doi.org/10.1007/BF00286077, 1996.

Bonini, M., Souriot, T., Boccaletti, M., and Brun, J.-P.: Successive orthogonal and oblique extension episodes in a rift zone: Laboratory experiments with application to the Ethiopian Rift, Tectonics, 16, 347–362, https://doi.org/10.1029/96TC03935, 1997.

Bonini, L., Fracassi, U., Bertone, N., Maesano, F. E., Valensise, G., and Basili, R.: How do inherited dip-slip faults affect the development of new extensional faults? Insights from wet clay analog models, J. Struct. Geol., 169, 104836, https://doi.org/10.1016/j.jsg.2023.104836, 2023.

Boutelier, D., Schrank, C., and Regenauer-Lieb, K.: 2-D finite displacements and strain from particle imaging velocimetry (PIV) analysis of tectonic analogue models with TecPIV, Solid Earth, 10, 1123–1139, https://doi.org/10.5194/se-10-1123-2019, 2019.

Brun, J.-P.: Narrow rifts versus wide rifts: inferences for the mechanics of rifting from laboratory experiments, Philos. T. Roy. Soc. A, 357, 695–712, https://doi.org/10.1098/rsta.1999.0349, 1999.

Brun, J.-P.: Deformation of the continental lithosphere: Insights from brittle-ductile models, Geol. Soc. Lond. Spec. Publ., 200, 355–370, https://doi.org/10.1144/GSL.SP.2001.200.01.20, 2002.

Brune, S., Corti, G., and Ranalli, G.: Controls of inherited lithospheric heterogeneity on rift linkage: Numerical and analogue models of interaction between the Kenyan and Ethiopian rifts across the Turkana depression, Tectonics, 36, 1767–1786, https://doi.org/10.1002/2017TC004739, 2017.

Buck, R. W.: Consequences of Asthenospheric Variability on Continental Rifting, in: Rheology and Deformation of the Lithosphere at Continental Margins, edited by: Karner, G. D., Taylor, B., Driscoll, N. W., and Kohlstedt, D. L., Columbia University Press, New York, USA, 1–30, https://doi.org/10.7312/karn12738-002, 2004.

Buck, R. W.: The role of magma in the development of the Afro-Arabian Rift System, Geol. Soc. Spec. Publ., 259, 43–54, https://doi.org/10.1144/GSL.SP.2006.259.01.05, 2006.

Buiter, S. J. H., Pfiffner, O. A., and Beaumont, C.: Inversion of extensional sedimentary basins: A numerical evaluation of the localisation of shortening, Earth Planet. Sc. Lett., 288, 492–504, https://doi.org/10.1016/j.epsl.2009.10.011, 2009.

Burov, E. and Cloetingh, S.: Erosion and rift dynamics: new thermomechanical aspects of post-rift evolution of extensional basins, Earth Planet. Sc. Lett., 150, 7–26, https://doi.org/10.1016/S0012-821X(97)00069-1, 1997.

Byerlee, J.: Friction of Rocks, Pure Appl. Geophys., 116, 615–626, https://doi.org/10.1007/BF00876528, 1978.

Calais, E., Ebinger, C., Hartnady, C., and Nocquet, J. M.: Kinematics of the East African Rift from GPS and earthquake slip vector data, Geol. Soc. Lond. Spec. Publ., 259, 9–22, https://doi.org/10.1144/GSL.SP.2006.259.01.03, 2006.

Carlo AG: Carlo Bernasconi AG, Switzerland, company website, http://www.carloag.ch, last access: 29 November 2022.

Chorowicz, J.: The East African rift system, J. Afr. Earth. Sci., 43, 379–410, https://doi.org/10.1016/j.jafrearsci.2005.07.019, 2005.

Corti, G.: Evolution and characteristics of continental rifting: Analog modeling-inspired view and comparison with examples from the East African Rift System, Tectonophysics, 522–523, 1–33, https://doi.org/10.1016/j.tecto.2011.06.010, 2012

Corti, G., Van Wijk, J., Cloetingh, S., and Morley, C. K.: Tectonic inheritance and continental rift architecture: Numerical and analogue models of the East African Rift system, Tectonics, 26, TC6006, https://doi.org/10.1029/2006TC002086, 2007.

Cowie, P. A., Underhill, J. R., Behn, M. D., Lin, J., and Gill, C. E.: Spatio-temporal evolution of strain accumulation derived from multi-scale observations of Late Jurassic rifting in the northern North Sea: A critical test of models for lithospheric extension, Earth Planet. Sc. Lett., 234, 401–419, https://doi.org/10.1016/j.epsl.2005.01.039, 2005.

Daly, M. C., Green, P., Watts, A. B., Davies, O., Chibesakunda, F., and Walker, R.: Tectonics and Landscape of the Central African Plateau and their Implications for a Propagating Southwestern Rift in Africa, Geochem. Geophys. Geosyst., 21, e2019GC008746, https://doi.org/10.1029/2019GC008746, 2020.

Delvaux, D., Kervyn, F., Macheyeki, A., and Temu, E: Geodynamic significance of the TRM segment in the East African Rift (W-Tanzania): Active tectonics and paleostress in the

Ufipa plateau and Rukwa basin, J. Struct. Geol., 37, 161–180, https://doi.org/10.1016/j.jsg.2012.01.008, 2012.

DeMets, C. and Merkouriev, S.: High-resolution estimates of Nubia–Somalia plate motion since 20 Ma from reconstructions of the Southwest Indian Ridge, Red Sea and Gulf of Aden, Geophys. J. Int., 207, 317–332, https://doi.org/10.1093/gji/ggw276, 2016.

DeMets, C. and Merkouriev, S.: Detailed reconstrucBons of India–Somalia Plate moBon, 60 Ma to present: implicaBons for Somalia Plate absolute moBon and India–Eurasia Plate moBon, Geophys. J. Int., 227, 1730–1767, https://doi.org/10.1093/gji/ggab295, 2021.

Ebinger, C. J.: Tectonic development of the western branch of the East African rift system, GSA Bull., 101, 885–903, https://doi.org/10.1130/0016-7606(1989)101<0885:TDOTWB>2.3.CO;2, 1989.

Ebinger, C. J.: Contental break-up: The East African perspective, Astron. Geophys., 46, 2.16–2.21, https://doi.org/10.1111/j.1468-4004.2005.46216.x, 2005.

Ebinger, C. J., Keir, D., Ayele, A., Calais, E., Wrigth, T. J., Belachew, M., Hammond, J. O. S., Campbell, E., and Buck, R. W.: Capturing magma intrusion and faulting processes during continental rupture: seismicity of the Dabbahu (Afar) rift, Geophys. J. Int., 174, 1138–1152, https://doi.org/10.1111/j.1365-246X.2008.03877.x, 2008.

Farangitakis, G.-P., SokouBs, D., McCaffrey, K. J. W., Willingshofer, E., Kalnins, L. M., Phethean, J. J. J., van Hunen, J., and Van Steen, V.: Analogue modeling of plate rotaBon effects in transform margins and ril-transform intersecBons, Tectonics, 38, 823–841, https://doi.org/10.1029/2018TC005261, 2019.

Farangitakis, G.-P., McCaffrey, K. J. W., Willingshofer, E., Allen, M. B., Kalnins, L. M., van Hunen, J., Persaud, P., and Sokoutis, D.: The structural evolution of pull-apart basins in response to changes in plate motion, Basin Res., 33, 1603–1625, https://doi.org/10.1111/bre.12528, 2021.

Glerum, A., Brune, S., Stamps, D. S., and Strecker, M. R.: Victoria continental microplate dynamics controlled by the lithospheric strength distribution of the East African Rift, Nat. Commun., 11, 2881, https://doi.org/10.1038/s41467-020-16176-x, 2020.

Globig, J., Fernàndez, M., Torne, M., Vergés, J., Robert, A., and Faccenna, C.: New insights into the crust and lithospheric mantle structure of Africa from elevation, geoid, and thermal analysis, J. Geophys. Res.-Sol. Ea., 121, 5389–5424, https://doi.org/10.1002/2016JB012972, 2016.

Henza, A. A., Withjack, M. O., and Schlische, R. W.: Normal-fault development during two phases of non-coaxial extension: An experimental study, J. Struct. Geol., 32, 1656–1667, https://doi.org/10.1016/j.jsg.2009.07.007, 2010.

Henza, A. A., Withjack, M. O., and Schlische, R. W.: How do the properties of a pre-existing normal-fault population influence fault development during a subsequent phase of extension?, J. Struct. Geol., 33, 1312–1324, https://doi.org/10.1016/j.jsg.2011.06.010, 2011.

Hieronymus, C. F.: Control on seafloor spreading geometries by stress- and strain-induced lithospheric weakening, Earth Planet. Sc. Lett., 222, 177–189, https://doi.org/10.1016/j.epsl.2004.02.022, 2004.

Hubbert, M. K.: Theory of scaled models as applied to the study of geological structures, Geol. Soc. Am. Bull., 48, 1459–1520, https://doi.org/10.1130/GSAB-48-1459, 1937.

Katz, R. F., Ragnarsson, R., and Bodenschatz, E.: Tectonic microplates in a wax model of sea-floor spreading, New J. Phys., 7, 37, https://doi.org/10.1088/1367-2630/7/1/037, 2005.

Keep, M. and McClay, K. R.: Analogue modelling of multiphase rift systems, Tectonophysics, 273, 239, https://doi.org/10.1016/S0040-1951(96)00272-7, 1997.

Kendall, J.-M. and Lithgow-Bertelloni, C.: Why is Africa rifting?, Geol. Soc. Lond. Spec. Publ., 420, 11–30, https://doi.org/10.1144/SP420.17, 2016.

Khalil, H. M., Capitanio, F. A., Betts, P. G., and Cruden, A. R.: 3-D Analog Modeling Constraints on Rifting in the Afar Region, Tectonics, 39, e2020TC006339, https://doi.org/10.1029/2020TC006339, 2020.

Kolawole, F., Firkins, M. C., Al Wahaibi, T. S., Atekwana, E. A., and Soreghan, M. J.: Rift interaction zones and the stages of rift linkage in active segmented continental rift systems, Basin Res., 33, 2984–3020, https://doi.org/10.1111/bre.12592, 2021a.

Kolawole, F., Phillips, T. B., Atekwana, E. A., and Jackson, C. A.-L.: Structural Inheritance Controls Strain Distribution During Early Continental Rifting, Rukwa Rift, Front. Earth Sci., 9, 707869, https://doi.org/10.3389/feart.2021.707869, 2021b.

Le Calvez, J. H. and Vendeville, B. C.: Experimental designs to model along-strike fault interaction, J. Virtual Explor., 7, 1–17, https://doi.org/10.3809/jvirtex.2002.00043, 2002.

Lezzar, K. E., Tiercelin, J. -J., Le Turdu, C., Cohen, A. S., Reynolds, D., J., Le Gall, B., and Scholz, C. A.: Control of Normal Fault Interaction on the Distribution of Major Neogene Sedimentary Depocenters, Lake Tanganyika, East African Rift, AAPG Bull., 86, 1027–1059, https://doi.org/10.1306/61EEDC1A-173E-11D7-8645000102C1865D, 2002.

Macgregor, D.: History of the development of the East African Rift System: A series of interpreted maps through time, J. Afr. Earth. Sc., 101, 232–252, https://doi.org/10.1016/j.jafrearsci.2014.09.016, 2015.

Maestrelli, D., Montanari, D., Corti, G., Del Ventisette, C., Moratti, G., and Bonini, M.: Exploring the Interactions Between Rift Propagation and Inherited Crustal Fabrics Through Experimental Modeling, Tectonics, 39, e2020TC006211, https://doi.org/10.1029/2020TC006211, 2020.

Martin, A. K.: Propagating rifts: Crustal extension during continental rifting, Tectonics, 3, 611–617, https://doi.org/10.1029/TC003i006p00611, 1984.

Martin, A. K.: Opposite microplate rotations on the East African Rift: Similarity to double saloon door tectonics, J. Afr. Earth Sci., 198, 104803, https://doi.org/10.1016/j.jafrearsci.2022.104803, 2023.

Michon, L., Famin, V., and Quicelleur, X.: Evolution of the East African Rift System from trap-scale to plate-scale rifting, Earth. Sc. Rev., 231, 104089, https://doi.org/10.1016/j.earscirev.2022.104089, 2022.

Molnar, N. E., Cruden, A. R., and Betts, P. G.: Interactions between propagating rotational rifts and linear rheological heterogeneities: Insights from three-dimensional laboratory experiments, Tectonics, 36, 420–443, https://doi.org/10.1002/2016TC004447, 2017.

Molnar, N. E., Cruden, A. R., and Betts, P. G.: Unzipping continents and the birth of microcontinent, Geology, 46, 451–454, https://doi.org/10.1130/G40021.1, 2018.

Molnar, N. E., Cruden, A. R., and Betts, P. G.: Interactions between propagating rifts and linear weaknesses in the lower crust, Geosphere, 15, 1617–1640, https://doi.org/10.1130/GES02119.1, 2019.

Molnar, N. E., Cruden, A. R., and Betts, P. G.: The role of inherited crustal and lithospheric architecture during the evolution of the Red Sea: Insights from three dimensional analogue experiments, Earth. Planet. Sc. Lett., 544, 116377, https://doi.org/10.1016/j.epsl.2020.116377, 2020.

Mondy, L. S., Rey, P. f., Ducleaux, G., and Moresi, L.: The role of asthenospheric flow during rift propagation and breakup, Geology, 46, 103–106, https://doi.org/10.1130/G39674.1, 2018.

Morley, C. K.: Stress re-orientation along zones of weak fabrics in rifts: An explanation for pure extension in 'oblique' rift segments?, Earth Planet. Sc. Lett., 297, 667–673, https://doi.org/10.1016/j.epsl.2010.07.022, 2010.

Morley, C. K., Ngenoh, D. K., and Ego, J. K.: Introduction to the East African Rift System, in: Geoscience of Rift Systems – Evolution of East Africa, edited by: Morley, C. K., AAPG Studies in Geology, 44, 1–18, https://doi.org/10.1306/St44623C1, 1999.

Mulugeta, G.: Squeeze box in a centrifuge. Tectonophysics, 148, 323–335, https://doi.org/10.1016/0040-1951(88)90139-4, 1988.

Nelson, R. A., Patton, T. L., and Morley, C. K.: Rift-Segment Interaction and Its Relation to Hydrocarbon Exploration in Continental Rift Systems, AAPG Bull., 76, 1153–1169, https://doi.org/10.1306/BDFF898E-1718-11D7-8645000102C1865D, 1992.

Neuharth, D., Brune, S., Glerum, A., Heine, C., and Welford, J. K.: Formation of continental microplates through rift linkage: Numerical modeling and its application to the Flemish Cap and Sao Paulo Plateau, Geochem. Geophys. Geosyst., 22, e2020GC009615, https://doi.org/10.1029/2020GC009615, 2021.

Neuharth, D., Brune, S., Wrona, T., Glerum, A., Braun, J., and Yuan, X.: Evolution of rift systems and their fault networks in response to surface processes, Tectonics, 41, e2021TC007166, https://doi.org/10.1029/2021TC007166, 2022.

Oldenburg, D. W. and Brune, J. N.: An explanation for the orthogonality of ocean ridges and transform faults, J. Geophys. Res., 80, 2575–2585, https://doi.org/10.1029/JB080i017p02575, 1975.

Osagiede, E. E., Rosenau, M., Rotevatn, A., Gawthorpe, R., Jackson, C. A.-L., and Rudolf, M.: Influence of zones of pre-existing crustal weakness on strain localization and partitioning during rifting: Insights from analog modeling using high-resolution 3D digital image correlation, Tectonics, 40, e2021TC006970, https://doi.org/10.1029/2021TC006970, 2021.

Panien, M., Schreurs, G., and Pfiffner, A.: Mechanical behaviour of granular materials used in analogue modelling: insights from grain characterisation, ring-shear tests and analogue experiments, J. Struct. Geol., 28, 1710–1724, https://doi.org/10.1016/j.jsg.2006.05.004, 2006.

Phethean, J. J. J., Kalnins, L. M., van Hunen, J., Biffi, P. G., Davies, R. J., and McCaffrey, K. J. W.: Madagascar's escape from Africa: A high-resolution plate reconstruction for the Western Somali Basin and implications for superconti-

nent dispersal, Geochem. Geophys. Geosyst., 17, 5036–5055, https://doi.org/10.1002/2016GC006624, 2016.

Pizzi, A., Coltorti, M., Abebe, B., Disperati, L., Sacchi, G., and Salvini, R.: The Wonji fault belt (Main Ethiopian Rift): structural and geomorphological constraints and GPS monitoring, Geol. Soc. Spec. Publ., 259, 191–207, https://doi.org/10.1144/GSL.SP.2006.259.01.16, 2006.

Purcell, P. G.: Re-imagining and re-imaging the development of the East African Rift, Petrol. Geosci., 24, 21–40, https://doi.org/10.1144/petgeo2017-036, 2018.

Rajaonarison, T. A., Stamps, D. S., and Naliboff, J.: Role of Lithospheric Buoyancy Forces in Driving Deformation in East Africa From 3D Geodynamic Modeling, Geophys. Res. Lett., 48, e2020GL090483, https://doi.org/10.1029/2020GL090483, 2021.

Rajaonarison, T. A., Stamps, D. S., Naliboff, J., Nyblade, A., and Njinju, E. A.: A Geodynamic Investigation of Plume-Lithosphere Interactions Beneath the East African Rift, J. Geophys. Res.-Sol. Ea., 128, e2022JB025800, https://doi.org/10.1029/2022JB025800, 2023.

Ramberg, H.: Gravity, Deformation and the Earth's Crust, Academic Press, London, ISBN-10 0125768605, ISBN-13 978-0125768603, 1981.

Ring, U.: The East African Rift System, Austrian J. Earth. Sc., 107, 132–146, 2014.

Rudolf, M., Boutelier, D., Rosenau, M., Schreurs, G., and Oncken, O.: Rheological benchmark of silicone oils used for analog modeling of short- and long-term lithospheric deformation, Tectonophysics 684, 12–22, https://doi.org/10.1016/j.tecto.2015.11.028, 2016.

Saria, E., Calais, E., Altamimi, Z., Willis, P., and Farah, H.: A new velocity field for Africa from combined GPS and DORIS space geodetic Solutions: Contribution to the definition of the African reference frame (AFREF), J. Geophys. Res.-Sol. Ea., 118, 1677–1697, https://doi.org/10.1002/jgrb.50137, 2013.

Saria, E., Calais, E., Stamps, D. S., Delvaux, D., and Hartnady, C. J. H.: Present-day kinematics of the East African Rift, J. Geophys. Res.-Sol. Ea., 119, 3584–3600, https://doi.org/10.1002/2013JB010901, 2014.

Schmid, T., Schreurs, G., Warsitzka, M., and Rosenau, M.: Effect of sieving height on density and friction of brittle analogue material: Ring-shear test data of quarz sand used for analogue experiments in the Tectonic Modelling Lab of the University of Bern, GFZ Data Services [data set], https://doi.org/10.5880/fidgeo.2020.006, 2020.

Schmid, T. C., Schreurs, G., and Adam, J.: Characteristics of continental rifting in rotational systems: New findings from spatiotemporal high resolution quantified crustal scale analogue models, Tectonophysics, 822, 229174, https://doi.org/10.1016/j.tecto.2021.229174, 2022a.

Schmid, T. C., Schreurs, G., and Adam, J.: Rotational extension promotes coeval upper crustal brittle faulting and deep-seated rift-axis parallel flow: Dynamic coupling processes inferred from analog model experiments, J. Geophys. Res.-Sol. Ea., 127, e2022JB024434, https://doi.org/10.1029/2022JB024434, 2022b.

Scott, D. L., Rosendahl., B. R., Burgess, C. F., and Sander, S.: Comments on "variable extension in Lake Tanganyika" by C. K. Morley, Tectonics, 8, 647–650, https://doi.org/10.1029/TC008i003p00647, 1989.

Smith, J. V.: Infinitesimal kinematics of rotational rifting with reference to en echelon marginal faults in the Red Sea region, Tectonophysics, 222, 227–335, https://doi.org/10.1016/0040-1951(93)90050-T, 1993.

Souriot, T. and Brun, J. -P.: Faulting and block rotation in the Afar triangle, East Africa: The Danakil "crank-arm" model, Geology, 20, 911–914, https://doi.org/10.1130/0091-7613(1992)020<0911:FABRIT>2.3.CO;2, 1992.

Stamps, D. S., Calais, E., Saria, E., Hartnady, C., Nocquet, J.-M., Ebinger, C. J., and Fernandes, R. M.: A kinematic model for the East African Rift, Geophys. Res. Lett., 35, L05304, https://doi.org/10.1029/2007GL032781, 2008.

Stamps, D. S., Flesch, L. M., Calais, E., and Ghosh, A.: Current kinematics and dynamics of Africa and the East African Rift System, J. Geophys. Res.-Sol. Ea., 119, 5161–5186, https://doi.org/10.1002/2013JB010717, 2014.

Stamps, D. S., Kreemer, C., Fernandes, R., Rajaonarison, T. A., and Rombolamanana, G.: Redefining East African Rift System kinematics, Geology, 49, 150–155, https://doi.org/10.1130/G47985.1, 2021.

Steinberger, B. and Calderwood, A. R.: Models of large-scale viscous flow in the Earth's mantle with constraints from mineral physics and surface observations, Geophys. J. Int., 167, 1461–1481, https://doi.org/10.1111/j.1365-246X.2006.03131.x, 2006.

Sun, Z., Zhong, Z., Keep, M., Zhou, D., Cai, D., Li, X., Wu, S., and Jiang, J.: 3D analogue modelling of the South China Sea: A discussion on breakup pattern, J. Asian Earth Sci., 34, 544–556, https://doi.org/10.1016/j.jseaes.2008.09.002, 2009.

Sutra, E., Manatschal, G., Mohn, G., and Unternehr, P.: QuanBficaBon and restoraBon of extensional deformaBon along the Western Iberia and Newfoundland riled margins, Geochem. Geophys. Geosys., 14, 2575–2597, https://doi.org/10.1002/ggge.20135, 2013.

Tentler, T. and Acocella, V.: How does the initial configuration of oceanic ridge segments affect their interaction? Insights from analogue models, J. Geophys. Res., 115, B01401, https://doi.org/10.1029/2008JB006269, 2010.

Tron, V. and Brun, J.-P.: Experiments on oblique rifting in brittle-ductile systems, Tectonophysics, 188, 71–88, https://doi.org/10.1016/0040-1951(91)90315-J, 1991.

Wang, L., Maestrelli, D., Corti, G., Zou, Y., and Shen, C.: Normal fault reactivation during multiphase extension: Analogue models and application to the Turkana Depression, East Africa, Tectonophysics, 811, 228870, https://doi.org/10.1016/j.tecto.2021.228870, 2021.

Wedmore, L. N. J., Turner, T., Biggs, J., Williams, J. N., Sichingabula, H. M., Kabumbu, C., and Banda, K.: The Luangwa Rift Active Fault Database and fault reactivation along the southwestern branch of the East African Rift, Solid Earth, 13, 1731–1753, https://doi.org/10.5194/se-13-1731-2022, 2022.

Weijermars, R. and Schmeling, H.: Scaling of Newtonian and non-Newtonian fluid dynamics without inertia for quantitative modelling of rock flow due to gravity (including the concept of rheological similarity), Phys. Earth Planet. In., 43, 316–330, https://doi.org/10.1016/0031-9201(86)90021-X, 1986.

Wheeler, W. H. and Karson, J. A.: Extension and subsidence adjacent to a "weak" continental transform: An example from the Rukwa rift, East Africa,

Geolog, 22, 625–628, https://doi.org/10.1130/0091-7613(1994)022<0625:EASATA>2.3.CO;2, 1994.

Withjack, M. O. and Jamison, W. R.: Deformation produced by oblique rifting, Tectonophysics, 126, 99–124, https://doi.org/10.1016/0040-1951(86)90222-2, 1986.

Wolfenden, E., Ebinger, C., Yirgu, G., Renne, P. R., and Kelley, S. P.: Evolution of a volcanic rifted margin: Southern Red Sea, Ethiopia, GSA Bull., 117, 846–864, https://doi.org/10.1130/B25516.1, 2005

Zwaan, F. and Schreurs, G.: How oblique extension and structural inheritance influence rift segment interaction: Insights from 4D analog models, Interpretation, 5, SD119–SD138, https://doi.org/10.1190/INT-2016-0063.1, 2017.

Zwaan, F. and Schreurs, G.: Rift segment interaction in orthogonal and rotational extension experiments: Implications for the large-scale development of rift systems, J. Struct. Geol., 140, 104119, https://doi.org/10.1016/j.jsg.2020.104119, 2020.

Zwaan, F. and Schreurs, G.: Time-lapse imagery, digital image correlation (DIC) and topographic analysis of laboratory experiments simulating the evolution of the East African Rift System, GFZ Data Services [data set], https://doi.org/10.5880/GFZ.2.5.2023.002, 2023.

Zwaan, F., Schreurs, G., Naliboff, J., and Buiter, S. J. H.: Insights into the effects of oblique extension on continental rift interaction from 3D analogue and numerical models, Tectonophysics, 693, 239–260, https://doi.org/10.1016/j.tecto.2016.02.036, 2016.

Zwaan, F., Schreurs, G., and Adam, J.: Effects of sedimentation on rift segment evolution and rift interaction in orthogonal and oblique extensional settings: Insights from analogue models analysed with 4D X-ray computed tomography and digital volume correlation techniques, Global Planet. Change, 171, 110–133, https://doi.org/10.1016/j.gloplacha.2017.11.002, 2018a.

Zwaan, F., Schreurs, G., Gentzmann, R., Warsitzka, M., and Rosenau, M.: Ring-shear test data of quartz sand from the Tectonic Modelling Lab of the University of Bern (CH), V. 1, GFZ Data Services [data set], https://doi.org/10.5880/fidgeo.2018.028, 2018b.

Zwaan, F., Schreurs, G., Ritter, M., Santimano, T., and Rosenau, M.: Rheology of PDMS-corundum sand mixtures from the Tectonic Modelling Lab of the University of Bern (CH), V. 1, GFZ Data Services [data set], https://doi.org/10.5880/fidgeo.2018.023, 2018c.

Zwaan, F., Schreurs, G., and Buiter, S. J. H.: A systematic comparison of experimental set-ups for modelling extensional tectonics, Solid Earth, 10, 1063–1097, https://doi.org/10.5194/se-10-1063-2019, 2019.

Zwaan, F., Schreurs, G., and Rosenau, M.: Rift propagation in rotational versus orthogonal extension: Insights from 4D analogue models, J. Struct. Geol., 135, 103946, https://doi.org/10.1016/j.jsg.2019.103946, 2020.

Zwaan, F., Chenin, P., Erratt, D., Manatschal, G., and Schreurs, G.: Complex rift patterns, a result of interacting crustal and mantle weaknesses, or multiphase rifting? Insights from analogue models, Solid Earth, 12, 1473–1495, https://doi.org/10.5194/se-12-1473-2021, 2021.

Zwaan, F., Chenin, P., Erratt, D., Manatschal, G., and Scheurs, G.: Competition between 3D structural inheritance and kinematics during rifting: insights from analogue models, Basin Res., 34, 824–854, https://doi.org/10.1111/bre.12642, 2022.